The Astrophysical Journal Supplement Series, 224:28 (30pp), 2016 June doi:10.3847/0067-0049/224/2/28

THE *SPITZER*-HETDEX EXPLORATORY LARGE-AREA SURVEY

C. Papovich[1,2], H. V. Shipley[1,2,3], N. Mehrtens[1,2], C. Lanham[1], M. Lacy[4], R. Ciardullo[5,6], S. L. Finkelstein[7], R. Bassett[8], P. Behroozi[9], G. A. Blanc[10,11,12], R. S. de Jong[13], D. L. DePoy[1,2], N. Drory[7], E. Gawiser[14], K. Gebhardt[7], C. Gronwall[5,6], G. J. Hill[7], U. Hopp[15,16], S. Jogee[7], L. Kawinwanichakij[1,2], J. L. Marshall[1,2], E. McLinden[7], E. Mentuch Cooper[7], R. S. Somerville[14], M. Steinmetz[13], K.-V. Tran[1,2], S. Tuttle[7], M. Viero[17], R. Wechsler[17], and G. Zeimann[5,6,7]
[1] Department of Physics and Astronomy, Texas A&M University, College Station, TX, 77843-4242 USA; papovich@physics.tamu.edu, papovich@tamu.edu
[2] George P. and Cynthia Woods Mitchell Institute for Fundamental Physics and Astronomy, Texas A&M University, College Station, TX, 77843-4242 USA
[3] Department of Physics & Astronomy, Tufts University, 574 Boston Avenue Suites 304, Medford, MA 02155, USA
[4] North American ALMA Science Center, NRAO Headquarters, Charlottesville, VA 22903, USA
[5] Department of Astronomy and Astrophysics, The Pennsylvania State University, University Park, PA 16802, USA
[6] Institute for Gravitation and the Cosmos, The Pennsylvania State University, University Park, PA 16802, USA
[7] Department of Astronomy, The University of Texas at Austin, Austin, TX 78712, USA
[8] International Centre for Radio Astronomy Research, University of Western Australia, 7 Fairway, Crawley, WA 6009, Australia
[9] Space Telescope Science Institute, 3700 San Martin Drive, Baltimore, MD 21218
[10] Departamento de Astronomía, Universidad de Chile, Camino del Observatorio 1515, Las Condes, Santiago, Chile
[11] Centro de Astrofísica y Tecnologías Afines (CATA), Camino del Observatorio 1515, Las Condes, Santiago, Chile
[12] Visiting Astronomer, Observatories of the Carnegie Institution for Science, 813 Santa Barbara St, Pasadena, CA 91101, USA
[13] Leibniz-Institut für Astrophysik Potsdam (AIP), An der Sternwarte 16, D-14482 Potsdam, Germany
[14] Department of Physics and Astronomy, Rutgers, The State University of New Jersey, 136 Frelinghuysen Road, Piscataway, NJ 08854, USA
[15] Max-Planck-Institut für Extraterrestrische Physik, D-85741, Garching, Germany
[16] Univeristätssternwarte München, LMU Munich, Scheiner Strasse 1, D-81679 Munich, Germany
[17] Kavli Institute for Particle Astrophysics and Cosmology, Stanford University, 382 Via Pueblo Mall, Stanford, CA 94305, USA
Received 2015 October 14; accepted 2016 March 16; published 2016 June 8

ABSTRACT

We present post-cryogenic *Spitzer* imaging at 3.6 and 4.5 μm with the Infrared Array Camera (IRAC) of the *Spitzer*/HETDEX Exploratory Large-Area (SHELA) survey. SHELA covers $\approx$24 deg^2 of the Sloan Digital Sky Survey "Stripe 82" region, and falls within the footprints of the Hobby–Eberly Telescope Dark Energy Experiment (HETDEX) and the Dark Energy Survey. The HETDEX blind $R \sim 800$ spectroscopy will produce $\sim$200,000 redshifts from the Lyα emission for galaxies in the range $1.9 < z < 3.5$, and an additional $\sim$200,000 redshifts from the [O II] emission for galaxies at $z < 0.5$. When combined with deep *ugriz* images from the Dark Energy Camera, *K*-band images from NEWFIRM, and other ancillary data, the IRAC photometry from *Spitzer* will enable a broad range of scientific studies of the relationship between structure formation, galaxy stellar mass, halo mass, the presence of active galactic nuclei, and environment over a co-moving volume of $\sim$0.5 Gpc^3 at $1.9 < z < 3.5$. Here, we discuss the properties of the SHELA IRAC data set, including the data acquisition, reduction, validation, and source catalogs. Our tests show that the images and catalogs are 80% (50%) complete to limiting magnitudes of 22.0 (22.6) AB mag in the detection image, which is constructed from the weighted sum of the IRAC 3.6 and 4.5 μm images. The catalogs reach limiting sensitivities of 1.1 μJy at both 3.6 and 4.5 μm (1σ, for $R = 2''$ circular apertures). As a demonstration of the science, we present IRAC number counts, examples of highly temporally variable sources, and galaxy surface density profiles of rich galaxy clusters. In the spirit of the *Spitzer* Exploratory programs, we provide all of the images and catalogs as part of the publication.

Key words: catalogs – galaxies: clusters: general – infrared: galaxies – surveys

1. INTRODUCTION

The launch of the *Spitzer Space Telescope* (Werner et al. 2004) allowed for large surveys of galaxies at near-IR wavelengths, which are free from foreground terrestrial thermal emission and are sensitive to the rest-frame peak of the stellar emission in galaxies ($\lambda_{\rm rest} \sim 1.6$ μm) over redshifts $z \sim$ 1–2 (e.g., Eisenhardt et al. 2008; Papovich 2008; Muzzin et al. 2013b). During the cryogenic mission, *Spitzer* executed a variety of initial, wide-area surveys (e.g., Lonsdale et al. 2003; Ashby et al. 2009; Wilson et al. 2009), and the post-cryogenic ("warm") mission enabled much larger surveys with increasingly larger combinations of depth and area (Mauduit et al. 2012; Ashby et al. 2013a, 2013b, 2015; Labbé et al. 2013, 2015; Timlin et al. 2016; Baronchelli et al. 2016).

The size and depth of the near-IR imaging surveys carried out by *Spitzer* have expanded our knowledge of how dark matter halos accumulate baryons and convert them into stars. The physics governing this formation involves a range of complex processes (see the recent review by Somerville & Davé 2015, and references therein). The processes for the growth of galaxies include baryon and dark-matter accretion histories, gas cooling, star formation, and galaxy mergers, while the processes that inhibit this growth include energetic winds from massive stars and supernovae, radiation and kinematic feedback from active galactic nuclei (AGNs) and shock heating of gas in large dark matter halos. Distinguishing the importance of these different processes, and their dependence on halo and stellar mass, redshift, and environment is one of the main goals of galaxy formation theory.

Spitzer has allowed us to test some of the theoretical physical processes by comparing measurements of the galaxy stellar mass distribution with model predictions. These processes should manifest themselves as a function of galaxy stellar mass, halo mass, redshift, and environment. By connecting

galaxies to their halos, we can identify and constrain the relative importance of the physical processes responsible for galaxy growth at different stages of their evolution. For example, recent studies have attempted to measure the ratio of galaxy stellar mass to halo mass (SM–HM) as a function of halo mass (e.g., Moster et al. 2010, 2013; Leauthaud et al. 2012; Behroozi et al. 2013; Kravtsov et al. 2014). The SM–HM relation provides a powerful mechanism for connecting the predictions for the halo mass function (which is well understood, e.g., Springel et al. 2005; Tinker et al. 2008; Behroozi et al. 2010, 2013) to the observed stellar mass functions and mass-dependent spatial clustering of galaxies (e.g., Weinberg et al. 2004; Reddick et al. 2013; Hearin et al. 2014; Skibba et al. 2015).

Expanding tests of galaxy formation derived from the SM–HM relation requires observational measurements of galaxies over large areas to measure both the bulk statistics and scatter in the halo- and stellar-mass distributions. This drives the need for larger extragalactic surveys that cover areas containing the full range of environments in which galaxies form, and during the epochs when the physical processes manifest.

The post-cryogenic *Spitzer* mission has enabled such surveys. Here, we describe one such program, the *Spitzer*/HETDEX Exploratory Large Area (SHELA) survey, which is designed to measure the evolution of the nature of the SM–HM relation for galaxies over a large baseline in redshift, $1.9 < z < 3.5$. SHELA targets a $\approx 24\,\mathrm{deg}^2$ field in the Sloan Digital Sky Survey (SDSS) Stripe 82 field (Annis et al. 2014), and covers a portion of the footprint of the Hobby–Eberly Telescope (HET) Dark Energy eXperiment (HETDEX, Hill et al. 2008). The SHELA field contains a large amount of ground-based imaging, including *griz* data from the Dark Energy Survey, additional *ugriz* data from our own DECam imaging program (I. Wold et al. 2016, in preparation), *K*-band data from the NEWFIRM instrument (M. Stevans et al. 2016, in preparation), and data in the far-IR, sub-mm, and X-ray wavelengths (LaMassa et al. 2013a, 2013b; Viero et al. 2014). The large SHELA field covers nearly $0.5\,\mathrm{Gpc}^3$ in cosmological volume at both moderate redshifts, $0.5 < z < 2.0$, and at high redshifts, $2.0 < z < 3.5$, and opens the distant universe in the way that large-area, shallow surveys, such as the SDSS (Alam et al. 2015) have expanded our knowledge of the local universe. As an equatorial field, the SHELA field is accessible to terrestrial telescopes in both hemispheres, which gives it a high and lasting legacy value for studies of galaxy evolution, AGN, and large-scale structure.

1.1. Overview of Paper

Here, we present the overview of the *Spitzer*/Infrared Array Camera (IRAC) imaging data set and catalogs for SHELA. The outline for this paper is as follows. In Section 2, we describe the SHELA survey field and the survey strategy with the *Spitzer Space Telescope*. In Section 3, we describe the data reduction and mosaicking of the *Spitzer* data set, and we describe astrometric and photometric quality checks on the imaging data. In Section 4, we discuss the construction of the source catalog, and the catalog properties, including source completeness. We also discuss estimates of photometric errors. In Section 5, we discuss basic scientific results, including source number counts, temporally varying objects, and the galaxy surface density of rich clusters. In Section 6, we summarize the work.

Throughout, we denote photometric magnitudes measured in the IRAC channel 1 and channel 2 as [3.6] and [4.5], respectively. Unless stated otherwise, all magnitudes here are relative to the absolute bolometric (AB) system (Oke & Gunn 1983). For convenience, we provide conversions between the AB system and the system relative to Vega, $[3.6]_{\mathrm{AB}} - [3.6]_{\mathrm{Vega}} = 2.79$ mag and $[4.5]_{\mathrm{AB}} - [4.5]_{\mathrm{Vega}} = 3.26$ mag, derived from a comparison to the spectrum a A0V spectral type star. Users of the catalog may apply these to the flux densities in the catalog to convert them to the magnitude system relative to Vega. For any derived, physical quantity, we assume a cosmology with $\Omega_m = 0.3$, $\Omega_\Lambda = 0.7$, and $H_0 = 70\,\mathrm{km\,s^{-1}\,Mpc^{-1}}$, consistent with the *WMAP* seven-year data (Komatsu et al. 2011) and Planck 2013 data (Planck Collaboration et al. 2014).

1.2. Overview of Data Products

Included with this paper, we release science-quality versions of the reduced IRAC imaging and catalogs. All data products are available through the NASA/IPAC Infrared Science Archive (IRSA[18]). A full description of the imaging is given in Section 3.2, and the contents of our catalogs are detailed in Section 4. Users may wish to skip to those sections. Here, we provide a high-level overview and some recommendations for the use of these data.

The catalogs contain source flux densities and their associated errors in units of μJy, where the AB magnitude is then given by $m_{\mathrm{AB}} = 23.9 - 2.5\log(f_\nu/\mu\mathrm{Jy})$ (see Section 1.1). The catalog contains four different flux density measurements: one defined using a circular 4″ diameter aperture (extension `4ARCS`), one derived using a circular 6″ diameter aperture (extension `6ARCS`), one formed using each objects' isophotal apertures (extension `ISO`), and one created using an elliptical aperture defined from the objects' light profiles using the Kron (1980) definition (extension `AUTO`). Each of these flux estimates has an associated uncertainty. Note that we have used the IRAC point-response functions (PRFs; see Sections 3.4 and 3.5) to correct our finite aperture (i.e., the `4ARCS` and `6ARCS`) measurements for light falling outside the defined aperture; thus, these data should represent the total fluxes for point sources. In contrast, the isophotal aperture (i.e., `ISO`) measurements have *not* been corrected for missing light. (By definition, the flux densities measured in the Kron [`AUTO`] aperture are "total" and require no correction).

The choice of aperture will depend on the exact user requirements of the application. For faint point sources, we recommend using the flux densities measured in 4″-diameter apertures (`4ARCS`), as these data contain the fewest low signal-to-noise ratio (S/N) pixels, and hence have the highest S/N overall. For brighter objects, or sources more extended than ∼2″, the larger aperture measurements are more appropriate. When the choice is uncertain, we recommend that users compare the 4″-diameter aperture flux measurements with those derived using the other apertures and check for evidence of light loss.

2. FIELD AND SURVEY CHARACTERIZATION

2.1. HETDEX

HETDEX is a survey which will measure the redshifts of $8 \times \sim 10^5$ Lyα emitting galaxies (LAEs) between

[18] http://irsa.ipac.caltech.edu/data/SPITZER/SHELA

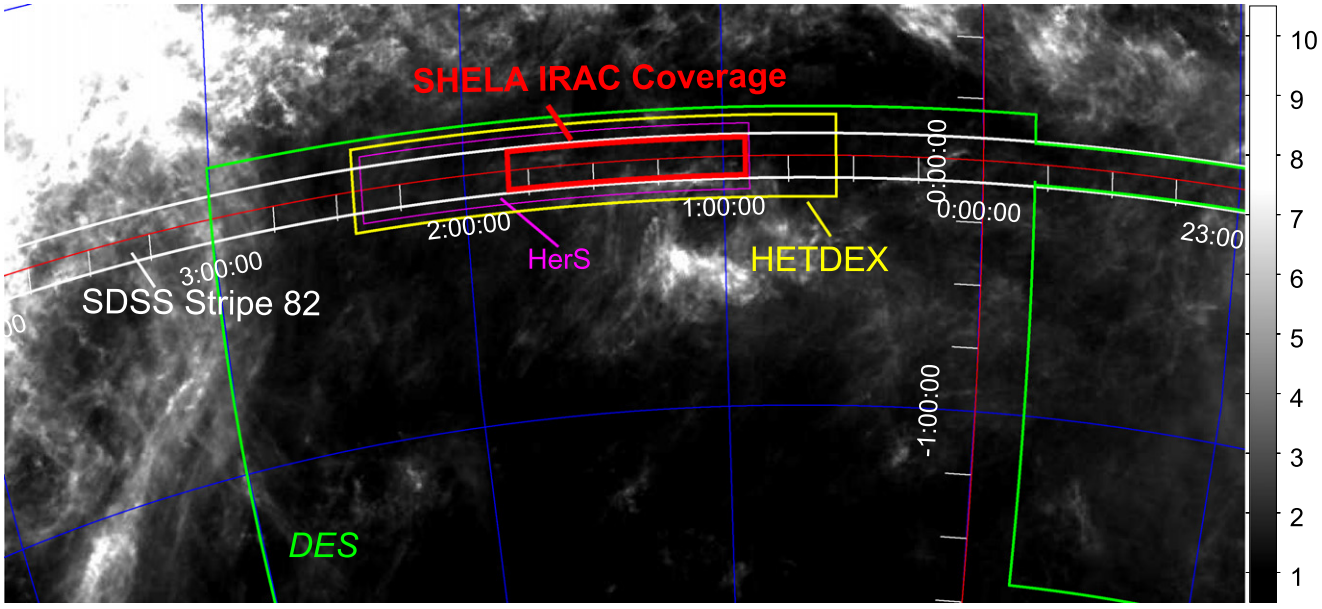

Figure 1. Field layout for SHELA. The lines show the coverage of our SHELA IRAC data (thick red-lined region), the SDSS Stripe 82 coverage (white-lined region), the planned coverage of the fall-field of the HETDEX survey (yellow-lined region), the HerS *Herschel* coverage (magenta-lined region) and the planned coverage of the DES (green-lined region). The lines of constant R.A. and decl. are labeled. The background image shows the IRAS 100 μm map of a portion of the south Galactic Pole (Schlegel et al. 1998). The image intensity scales with surface brightness as indicated in the color bar in units of MJy sr^{-1}.

$1.9 < z < 3.5$ using a suite of 78 wide-field integral field units (IFU) spectrographs covering the wavelength region 350–550 nm (Hill et al. 2008). The goal of these observations will be to provide sub-percent level measurements of the Hubble expansion parameter and the angular diameter distance at $z \sim 2$ via the large-scale distribution of galaxies in the redshift range of HETDEX. The result will be a significant constraint on the evolution of dark energy that is competitive with (and independent of) values based on surveys of the Lyα forest (e.g., Slosar et al. 2013; Delubac et al. 2015).

The entire HETDEX survey will cover 420 deg^2 with a 1/4.5 filling factor over two fields: a ~300 deg^2 northern field, and a ~140 deg^2 equatorial region. The ≈24 deg^2 SHELA field falls within the equatorial region, and, within its borders, HETDEX will increase its fill factor to unity (i.e., every portion of the SHELA field will be targeted for spectroscopy). The 10 σ detection limit for these spectra will be 3.4×10^{-17} ergs cm^{-2} s^{-1} at 500 nm, or equivalently for continuum objects, $g_{\rm AB} = 21.9$ mag.

Figure 1 shows the location of the equatorial HETDEX field and the SHELA field. The SHELA/IRAC imaging will detect >200,000 galaxies at $1.9 < z < 3.5$ down to a limiting stellar mass of ≃2–3 $\times 10^{10}$ $M_\odot$. Figure 2 shows how the SHELA IRAC 3σ flux limits compare to the spectrum of a star-forming galaxy at $z = 2.5$ (expected in both the LAE and non-LAE populations), including the effects of nebular emission lines (Salmon et al. 2015), and a spectrum of a passive galaxy at $z = 1.5$. The figure also shows the preliminary 3σ magnitude limits from our DECam data (I. Wold et al. 2016, in preparation) and NEWFIRM data (M. Stevans et al. 2016, in preparation) and the 50% completeness limits for the optical imaging in the SDSS Stripe 82 field (Annis et al. 2014). The combined depths of the optical (*ugriz*), near-IR (K_s), and mid-IR (3.6–4.5 μm) data will enable one to measure stellar masses of galaxies to down to these flux limits. This enables the goal the combined HETDEX-SHELA data set, which is measure the stellar masses $z \sim 2.5$ galaxies past the characteristic mass, M^*,

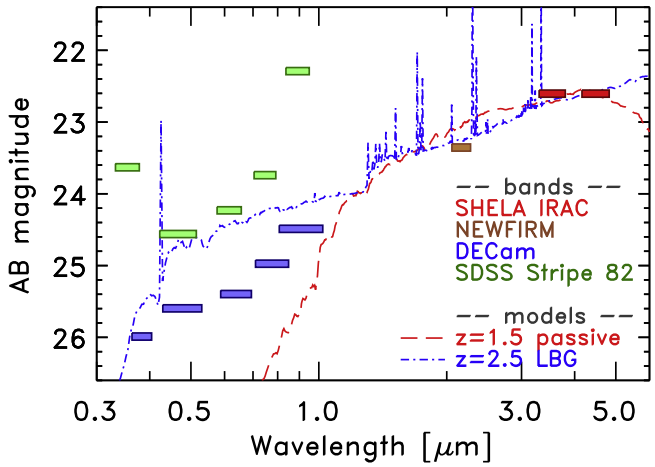

Figure 2. Comparison of optical and IR magnitude limits for the SHELA field compared with fiducial model stellar populations. The colored bars show the 3σ limits for the SHELA IRAC imaging derived in this paper, with preliminary values from our DECam and NEWFIRM imaging, as well as the 50% completeness limits for the SDSS Stripe 82 survey data. The curves show model stellar populations of a $z = 2.5$ star-forming "Lyman-break galaxy" (LBG) with stellar mass $\log(M/M_*) = 10$ and moderate extinction, $E(B-V) = 0.25$, and a $z = 1.5$ passively evolving galaxy with age $\log t/{\rm yr} = 9.3$ and stellar mass $\log(M/M_*) = 10.3$.

at these redshifts (e.g., Muzzin et al. 2013a; Tomczak et al. 2014). Moreover, the combined HETDEX-SHELA data set will enable the measurement of the relationship between halo mass (constrained by the HETDEX density field) and stellar mass (derived from the optical/IR photometry) over a survey volume large enough to minimize statistical uncertainties.

Results from the HETDEX pilot survey using a prototype of the HETDEX IFU on the McDonald 2.7 m illustrate the impact of joint spectroscopy and stellar-population modeling of the LAE populations in small-area fields where optical/near-IR imaging and *Spitzer*/IRAC imaging already exist. These include results published in Adams et al. (2011), Blanc et al.

(2011), Finkelstein et al. (2011), Hagen et al. (2014), and Chiang et al. (2015). The results of the pilot survey also give us confidence that we understand the properties of our LAE selection, including their luminosity function and our ability to select LAEs for HETDEX with little contamination.

2.2. Field Location and Ancillary Data

The SHELA field is centered at R.A. = $1^h22^m00^s$, decl. = $+00°00'00''$ (J2000), (Galactic coordinates, $l = 138.°294$, $b = -62.°017$) and extends approximately $\pm 6.°5$ in R.A. and $\pm 1.°25$ in decl. The field was chosen to have low IR background (Schlegel et al. 1998) within the SDSS Stripe 82 and DES fields. As illustrated in Figure 1, the 100 μm background ranges from 1.2 to 1.7 MJy sr^{-1} across the field, and with a mean value of approximately 1.5 MJy sr^{-1}.

Because of its equatorial location, the SHELA field lies near the Ecliptic ($\lambda = 18.°93$, $\beta = -8.°01$, and ranges in latitude from $\beta = -4°$ to $-11°$). Because the primary component of the background for *Spitzer*/IRAC is the Zodiacal light, this results in a higher background than higher (Ecliptic) latitude fields. The Ecliptic latitude for SHELA falls between the values assumed for the "medium" and "high" background in the *Spitzer* sensitivity performance estimation tool (SENS-PET).[19] Therefore, it is expected that the SHELA field will suffer higher-than average Zodiacal backgrounds, which adversely effects the flux sensitivity of the IRAC data.

An advantage of the equatorial location is that the SHELA field is readily observable by current and future optical/IR and radio telescopes. The SHELA field is centered on the equator, and overlaps with the DES optical imaging, and the optical imaging from the deeper SDSS/Stripe 82 coadd (Annis et al. 2014). These data are supplemented with our own deeper CTIO/DECam *ugriz* data, which reach 3σ limiting magnitudes of $u = 26.0$, $g = 25.6$, $r = 25.4$, $i = 25.0$, and $z = 24.5$ (in 2″-diameter apertures). In addition, the field is being imaged in the K_s band down to a 5σ depth of 22.8 mag using the NEWFIRM camera at Kitt Peak (PI: S. Finkelstein). The DECam and NEWFIRM limits are illustrated in Figure 2. The SHELA field also has 250, 350, and 500 μm images from the SPIRE instrument taken as part of the *Herschel* Stripe 82 Survey (HerS, Viero et al. 2014), and X-ray coverage from *Chandra* and *XMM-Newton* (LaMassa et al. 2013a, 2013b). Finally, the SHELA field has received microwave observations at 148, 218, and 270 GHz from the Equatorial Survey of the Atacama Cosmology Telescope (ACT, Hasselfield et al. 2013). The growing amount of multiwavelength data makes SHELA a unique resource for the study of physical properties of evolution of galaxies as a function of environment.

Additional *Spitzer*/IRAC imaging of the SDSS Stripe 82 field exists from the *Spitzer* IRAC Equatorial Survey (SpIES, proposal ID (PID) 90045, PI: G. Richards; Timlin et al. 2016). The SpIES data cover an additional $\sim$115 deg^2 outside the SHELA footprint along SDSS Stripe 82, with an effective IRAC integration time of 120 s. Scaling by integration times, the SHELA data are approximately $2.5\log(\sqrt{270/120}) = 0.44$ mag deeper than SpIES. The reader is referred to Timlin et al. (2016), for a description of SpIES and its data products.

[19] http://ssc.spitzer.caltech.edu/warmmission/propkit/pet/senspet

Table 1
Observation Log for IRAC Observations

Observing Epoch (1)	Observing Dates (UTC) (2)	Position Angles (deg. E of N) (3)	Number of AORS (4)
1	2011 Sep 28 to 2011 Oct 10	−110.0 to −105.5	64
2	2012 Feb 13 to 2012 Feb 29	63.1 to 65.3	63
3	2012 Sep 28 to 2012 Oct 09	−110.9 to −107.4	64

2.3. SHELA IRAC Survey Strategy

IRAC (Fazio et al. 2004b) observes simultaneously in channel 1 (at 3.6 μm) and channel 2 (at 4.5 μm), with each channel covering a $5.'2 \times 5.'2$ field. The field centers observed by each channel are separated on the sky by approximately 6.7 arcmin, with a gap of about 1.52 arcmin between the fields. We designed the mapping strategy for SHELA to obtain coverage in both channels over approximately the same area of sky.

Several constraints affected the design of our survey. We desired multiple dithers with slightly different position angles to allow redundancy, to identify cosmic rays, and to guard against image defects. We desired observations during several epochs to ease *Spitzer* scheduling requirements. The multiple epochs are separated by long enough periods of time (approximately 4–7 months) to identify time-variable objects including asteroids (as our observations are close to the ecliptic we expect asteroids to be detected at higher rates than higher-latitude extragalactic fields). We also required that all astronomical observation requests (AORs) be shorter than the maximum observing time, about 6 hr for *Spitzer*.

We divided the SHELA observations into three epochs, separated by approximately six months. There were two, 30-day duration observing windows each year for *Spitzer* to observe SHELA at position angles optimal for our survey strategy.

During each epoch we observed the entire SHELA field to one-third of the total depth, covering approximately 12×2.5 deg^2. Each AOR used a three point dither pattern, with 1×30 s frame time per position (where the array observes with 23.6 s of exposure time for a 30 s frame). Each AOR obtained a map divided into 8 rows by 10 columns of IRAC pointings, with a step size of 280″ between each pointing. The area covered by each AOR is approximately $38' \times 47'$, and each epoch tiled the entire SHELA field using 64 AORS (epochs 1 and 3) or 63 AORs (epoch 2). A single AOR required approximately 2.75 hr of clock time. As there are 191 AORs, the total clock time for SHELA required 525 hr of *Spitzer* observations. The *Spitzer* observations of SHELA occurred in the three epochs using these AORS under program PID 80100 (PI: Papovich), with dates listed in Table 1. The table also gives the position angles of IRAC during the observations and the number of AORs observed during each epoch.

3. IRAC DATA

3.1. Data Reduction

The SHELA IRAC data reduction began with the data pipeline processing version S19.0.0 of the IRAC Corrected Basic Calibrated Data (cBCD) provided by the *Spitzer* Science Center (SSC). The data processing includes a subtraction of the

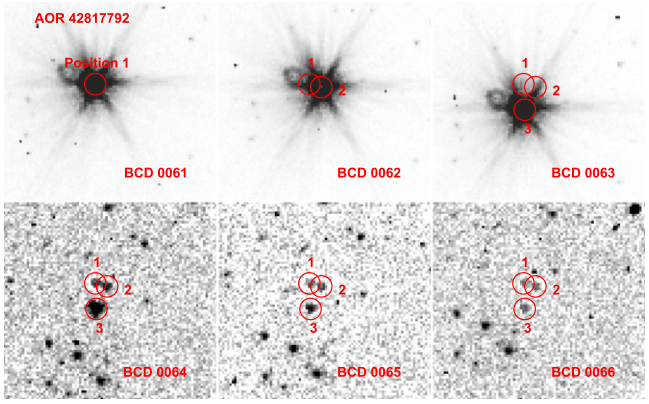

Figure 3. Example of persistence in the IRAC 3.6 μm data. The data are from AOR 42817792 of SHELA. Each panel shows the same region of the IRAC detector in a time series of sequential BCDs, from 0061 to 0066. In the first three BCDs (0061–0063), the bright star (HD 9670, $V = 6.9$ mag) falls at position 1, 2, and 3 in this portion of the IRAC detector. The bright star leaves a fractionally small persistence effect (<0.01% of the fluence) in the same x, y pixels in subsequent BCDs (0064–0066), which decays with an exponential timescale.

dark current and application of the flat field, as well as a photometric and astrometric calibration. Starting with the cBCD products, we next applied several steps to correct for variations and features in the image backgrounds. We corrected each image for column-pulldown effects associated with bright sources using custom software ("fixpulldown.pro").[20] We next constructed a median frame from all cBCDs in a single AOR, clipping outliers. In this way we make a sky frame from all images in an AOR. We subtracted this image from each individual cBCD to eliminate structure and residuals. We then removed additional striping in the backgrounds by averaging over five columns in each image (clipping for objects), and subtracted this from each column. We also excluded the first frame from each series of exposures in a given AOR sequence to remove any variable instrument bias level associated with idiosyncrasies of the post-cryogenic IRAC electronics (the "first frame effect"[21]).

Our inspection of preliminary reductions showed some instances where persistence from bright stars produced spurious sources in the final mosaics. This occurs even though the data-reduction pipeline flags for image persistence (and we set persistence-flagged pixels as "fatal" during the mosaic stage, see below), and suspect this occurs because the pipeline flags only persistence from the brightest objects (and fainter objects, which still cause persistence, are missed). Figure 3 shows an example of the persistence caused by a bright star (HD 9670, $V = 6.9$ mag) in a consecutive series of cBCDs from one of the SHELA AORs. Following our observing strategy, the star is dithered to 3 different positions on the detector, before the IRAC array is stepped to a new location on the sky. The persistence from the star is evident in several subsequent exposures. The persistence fades with an exponential timescale (as expected for trapped electron decay rates) and is mainly a problem in the 3.6 μm images (it is nearly negligible in the 4.5 μm images, see footnote 21).

[20] http://irsa.ipac.caltech.edu/data/SPITZER/docs/dataanalysistools/tools/contributed

[21] See the IRAC Instrument Handbook (2015, version 2.1), available at: http://irsa.ipac.caltech.edu/data/SPITZER/docs/irac/iracinstrumenthandbook.

To correct for the strongest persistence residuals, one of us (CL) inspected visually each channel 1 cBCD sequentially in the order they were observed, identifying persistence events. We then flagged those pixels with persistence using the locations of the bright objects in the previous cBCDs in the observing sequence. We combined these flag maps with the mask files produced by the SSC pipeline and included the masked pixels as fatal bits in the mosaicking steps. Even so, we have likely not accounted for all possible persistence in the images. Persistence can manifest as "sources" that vary in the time domain between observations in different epochs, and users of the catalogs (especially for time-domain studies or sources detected in a single channel of an observing epoch) should be wary that some time-variable sources may be a result of faint persistence missed by our inspection of the images.

3.2. Image Mosaics

We used a combination of the MOPEX software (v18.5.4) provided by the SSC[22] and SWarp (v2.19.1 Bertin et al. 2002) to produce mosaics of the IRAC data. Our choice to use SWarp is a result of the fact that the memory limitations of MOPEX are too stringent for a data set with the size of the SHELA data volume. We first produced a mosaic for each AOR separately using MOPEX. MOPEX includes full propagation of errors for each pixel and masks pixels set to fatal bit patterns (including pixels we estimate to contain persistence, see above).

We next used SWarp to mosaic the output from MOPEX for each AOR into images covering the full SHELA field. We employed a background subtraction with `BACK_SIZE = 128` and `BACK_FILTERSIZE = 3` within SWarp to account for (small) offsets in the backgrounds between AORs. We combined AORs using a weighted average (`COMBINE_TYPE = WEIGHTED`) from the exposure-time maps for each AOR, and we resampled the images to a common field center and pixel scale of $0\farcs8$ pixel^{-1}. We produced full mosaics of all the data at 3.6 and 4.5 μm. We also produced mosaics in each channel in each of the 3 observing epochs separately. Figures 4 and 5 show the combined, three-epoch mosaics at 3.6 and 4.5 μm, respectively.

We also combined the weight maps using SWarp. Figures 4 and 5 show the weight map coverage for the full mosaic at 3.6 and 4.5 μm, respectively. The values in the weight map correspond to the number of IRAC exposures for each pixel on the sky, and the weight map is therefore proportional to the effective exposure time, $t_{\rm eff} = 23.6\ {\rm s} \times W$, where W is the value of the weight map. Figure 6 shows the distribution of area covered to a given exposure time in the 3.6 μm and 4.5 μm full mosaics compared to the coverage from epoch 1 only. A single epoch covers a 26 deg^2 area with three pointings from the dither pattern ($W = 3$), for an effective exposure time, $t_{\rm eff} \simeq 71$ s. The full mosaic covers an area of 30 deg^2 with $W = 6$ pointings ($t_{\rm eff} = 142$ s depth), 24.2 deg^2 with $W = 8.5$ pointings ($t_{\rm eff} > 200$ s depth), and 22.4 deg^2 with $W > 9$ pointings reaching the full survey depth ($t_{\rm eff} > 212$ s depth).

3.3. Astrometric Quality

In preliminary versions of the SHELA IRAC mosaics, we identified small astrometric offsets between cBCDs from

[22] http://irsa.ipac.caltech.edu/data/SPITZER/docs/dataanalysistools/tools

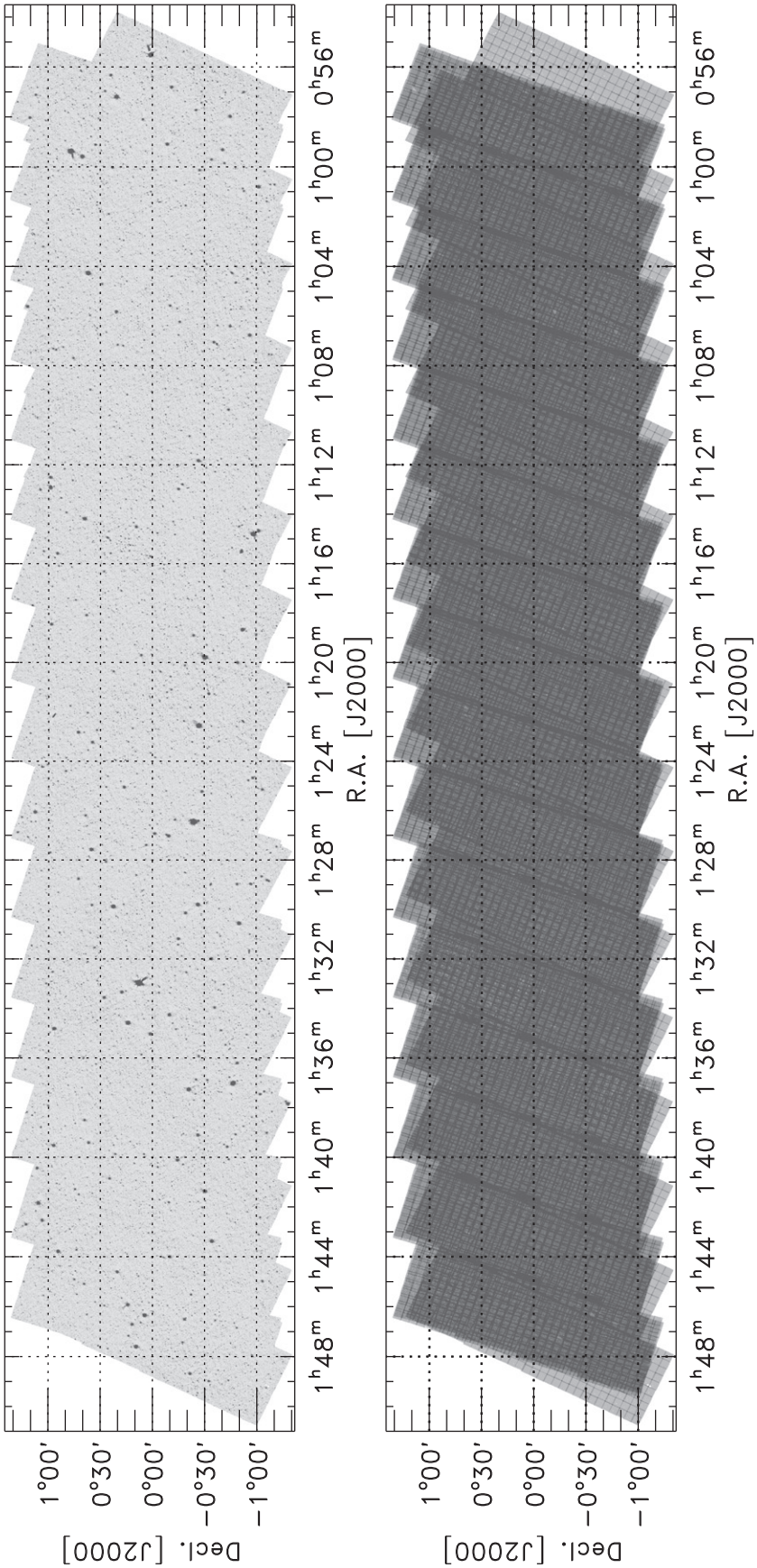

Figure 4. Combined, three-epoch mosaic of the SHELA IRAC Channel 1 (3.6 μm) data (left) and associated exposure-time (weight) map (right). The extreme edges of the image cover nearly $2.^{\circ}5 \times 13^{\circ}$, but the area covered to our 3-epoch depth is $\approx$24 deg^2.

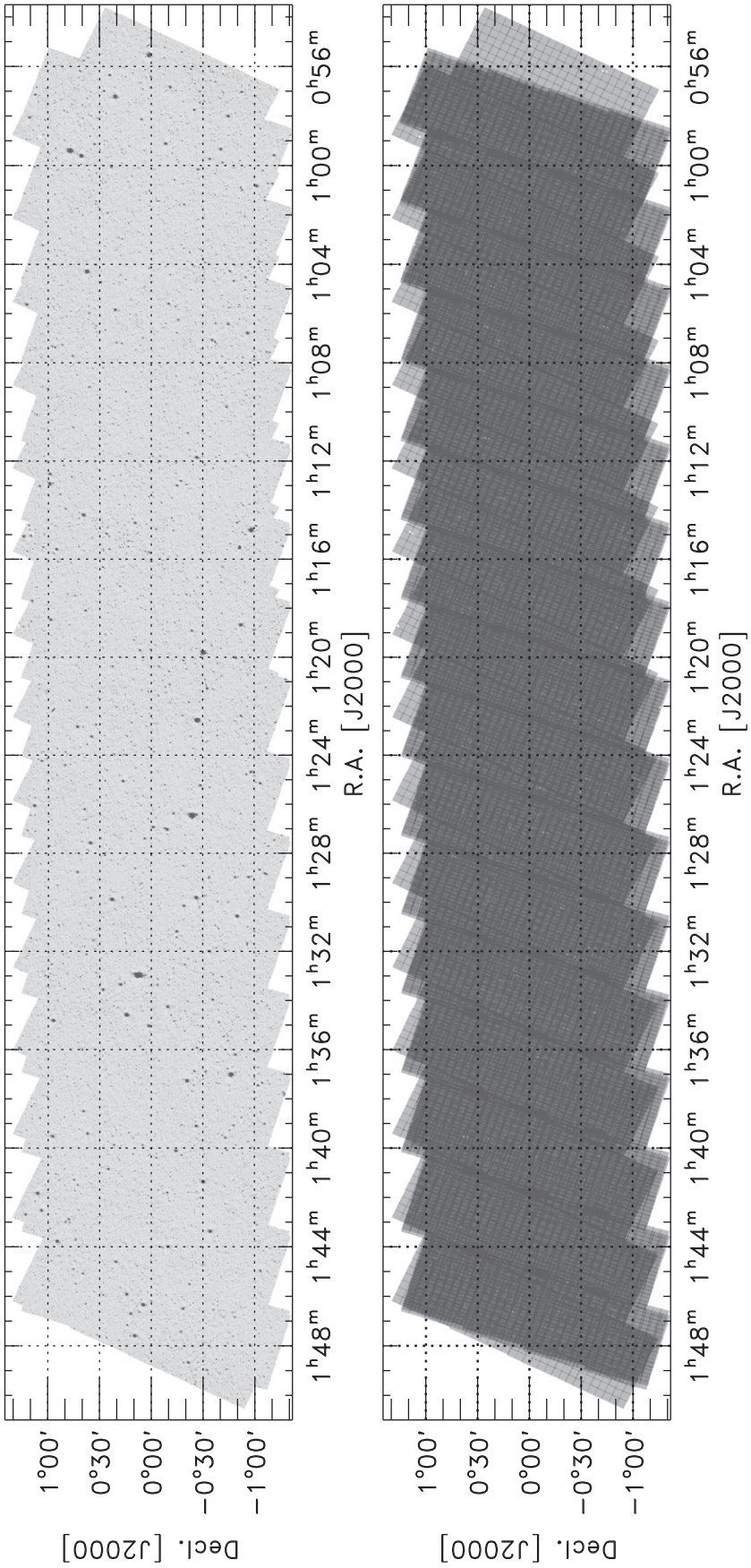

Figure 5. Same as Figure 4, but for the SHELA IRAC Channel 2 (4.5 μm) data (left) and the associated exposure-time (weight) map (right).

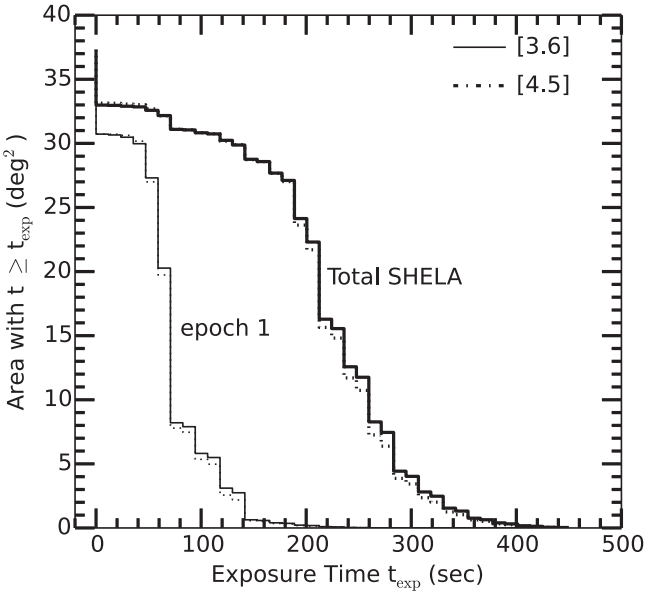

Figure 6. Cumulative distribution of area with exposure times $\geqslant t_{\rm exp}$. The thin lines show the distribution only for the first epoch IRAC data, and the thick lines show the distribution for the combined three epoch data. The solid lines show the 3.6 μm distribution and the dotted line shows the 4.5 μm distribution.

different AORs. On subsequent re-reductions, we corrected for these inter-AOR shifts using multiple tests.

We computed coarse astrometric offsets by cross-correlating the positions of objects in each cBCD with sources detected in the SDSS DR7 (Abazajian et al. 2009) catalog and updating the image headers. The astrometric offsets were mostly small, with shifts of up to $\approx 0\farcs2$ in both R.A. and decl. We then combined all cBCDs from all mosaics from each epoch, and we again checked the absolute astrometry of each mosaic, using the newer SDSS DR7 as a reference frame. Finally, we corrected for the remaining (small) relative shifts between each individual epoch. Compared to SDSS DR7 the offsets of the 3.6 μm images were: $\Delta\alpha = \alpha_{\rm SHELA} - \alpha_{\rm DR7} = -140, +180, -140$ mas, and $\Delta\delta = \delta_{\rm SHELA} - \delta_{\rm DR7} = +60, -80, +50$ mas, for epochs 1, 2, and 3, respectively. The offsets to the 4.5 micron images were slightly different: $\Delta\alpha = -134, +140, -130$ mas; and $\Delta\delta = -140, +110, -150$ mas, for epochs 1, 2, and 3, respectively. The origin of the offsets is unclear, but may be related to the errors measured in the positions of the stars in the *Spitzer* star trackers for the different spacecraft orientations (where the errors may be a combination of uncertainties in the proper motions in the guide star catalog, proper motions of stars in the 2MASS catalog used for the pointing refinement step of the IRAC pipeline, and intrapixel sensitivity variations that add noise to the measured star positions). The orientation of epochs 1 and 3 were approximately the same, while the spacecraft orientation for epoch 2 was different by approximately 180°, and indeed, the largest offsets were between epoch 1 and 2 and epochs 2 and 3 (see above). We corrected for these astrometric offsets between each epoch before combining the data into the final mosaics. Our tests showed that correcting for astrometric shifts for each epoch improved the image quality of point sources in the final mosaic.

We remosaicked all the data using the improved astrometric corrections. As a result, the final astrometric solutions are very good compared to SDSS DR7. Figure 7 shows that offsets between SHELA and DR7 are indeed very small, $\Delta\alpha = \alpha_{\rm SHELA} - \alpha_{\rm DR7} = -14$ mas and $\Delta\delta = \delta_{\rm SHELA} - \delta_{\rm DR7} = 7$ mas. For comparison, the scatter is $\sigma(\alpha) = 180$ mas and $\sigma(\delta) = 160$ mas in each dimension. The scatter is comparable to the quoted uncertainty in the SDSS DR7 astrometric solution (Abazajian et al. 2009). We also rechecked the astrometry between SHELA and the newer SDSS DR9 coordinates, and obtained similar values, with systematic shifts of $\Delta\alpha = -23$ mas and $\Delta\delta = 18$ mas, and an overall scatter of $\sigma(\alpha) = 160$ mas and $\sigma(\delta) = 150$ mas. The slight increase in the offset between DR7 and DR9 is well within the uncertainty in the absolute astrometric calibration of SDSS (Ivezić et al. 2007). The offsets are also small between SDSS DR7 and the IRAC images from each individual epoch.

We also compared the astrometry between SHELA and the 2MASS all-sky point-source catalog (Skrutskie et al. 2006). There are very small shifts of $\Delta\alpha = -8$ mas and $\Delta\delta = -30$ mas, with scatter $\sigma(\alpha) = 270$ mas and $\sigma(\delta) = 260$ mas in each dimension. This is larger than the typical positional uncertainty for $K_s < 14$ mag sources ($\lesssim$100 mas, Skrutskie et al. 2006), but we have made no correction for proper motion of stars, and the accuracy is consistent with that reported in Sanders et al. (2007), who state an accuracy of ~200 mas for their *Spitzer* IRAC data.

There are larger shifts between the SHELA IRAC astrometry and the astrometry of point sources in the AllWISE catalog (Cutri et al. 2013). Figure 7 shows that the offsets are $\Delta\alpha = -53$ mas and $\Delta\delta = 69$ mas, with scatter of $\sigma(\alpha) = 190$ mas and $\sigma(\delta) = 200$ mas in each dimension. The scatter is consistent with the astrometric uncertainty of the AllWISE catalogs (Cutri et al. 2013), but the larger offsets in the astrometry (approaching a tenth of an arcsecond) may be non-negligible for some applications.

3.4. Point Response Functions

For a variety of quality tests of the data and catalogs, it is useful to have an empirical PRF for the 3.6 and 4.5 μm images. In each SHELA image, we identified point sources from the AllWISE catalog brighter than $W1 < 15$ Vega mag with flag value $\mathtt{ex} = 0$. We kept objects only in the magnitude range $14 < W1 < 15$ Vega mag as these have high signal to noise, are well away from being saturated, and because brighter objects are weighted more in the construction of the PRF. We constructed average PRFs using the routines provided in IDLPhot,[23] which is based on the DAOPhot software (Stetson 1987). Figure 8 shows the PRFs for the 3.6 and 4.5 μm data.[24]

We use the empirical PRF for tests of object photometric accuracy and completeness in Sections 4.1 and 4.2 below. We measure a full-width at half maximum (FWHM) of $1\farcs97$ and $1\farcs99$ from Gaussian fits to the 3.6 and 4.5 μm PRFs, respectively. These agree with the expected values at the native IRAC pixel scale for the IRAC channel 1 and 2 detectors during the warm mission.[25]

We measured a curve-of-growth of the PRFs using circular apertures and compared those to the flux measured with the

[23] http://idlastro.gsfc.nasa.gov/ftp/pro/idlphot

[24] FITS versions of these PRFs are available through IRSA, see http://irsa.ipac.caltech.edu/data/SPITZER/SHELA/prfs.

[25] Data taken with IRAC during the warm *Spitzer* mission have measured FWHMs for the PRFs ≈15% larger than for data taken during the the cold *Spitzer* mission, see the IRAC instrument handbook, link in footnote 21.

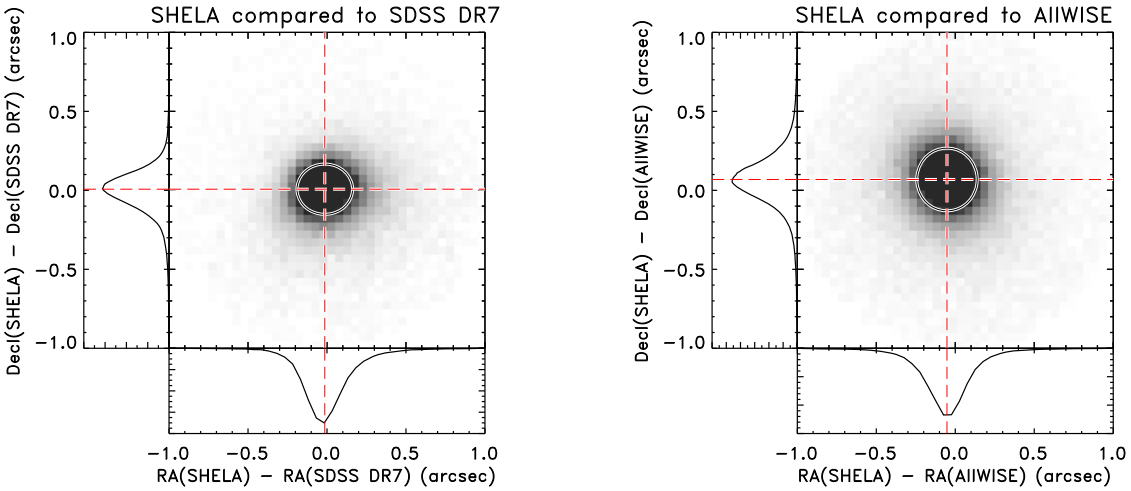

Figure 7. Astrometric comparison for point sources between the SHELA/IRAC and SDSS DR7 (left panel) and between SHELA/IRAC and AllWISE (right panel). In each main plot, the shading is proportional to the density of objects in each region of the plot. The subpanels of each plot show the distributions of the differences in R.A. and decl., separately. The red, dashed lines show the mean offset. The ellipses contain 68% of the sources. There are negligible offsets between SDSS DR7 and SHELA (by construction), and the scatter is consistent with the SDSS astrometric accuracy of $0\farcs2$ (Abazajian et al. 2009). In contrast, the AllWISE astrometry has a non-negligible offset of ≈60–70 mas in both R.A. and decl., with a scatter of $0\farcs2$ in each dimension.

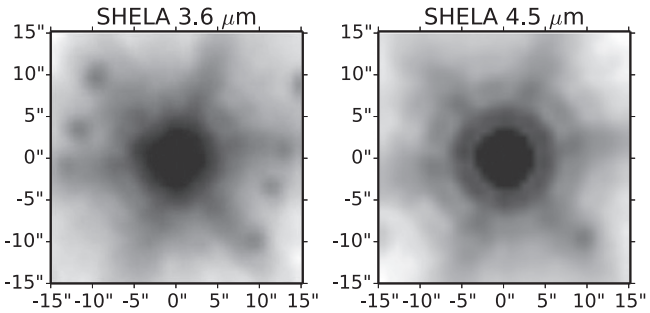

Figure 8. Empirical PRFs for the SHELA IRAC 3.6 and 4.5 μm data. The PRFs are constructed by combining the IRAC fluxes for point sources from the AllWISE catalog with magnitudes $14 < W1 < 15$ Vega mag.

fiducial IRAC aperture (radius $R = 12''$) used to derive the IRAC flux calibration (see the IRAC Instrument Handbook, link in footnote 21). The curve of growth provides an estimate of the amount of light lost outside the photometric aperture. For large apertures ($R > 2''$) these corrections are identical to the ones we adopt below (Section 3.5), but they differ at the 0.05–0.10 mag level for apertures $R < 1$–$2''$.

3.5. Photometric Aperture Corrections

Because we used the SExtractor software package for object photometry in our SHELA catalog (Section 4, below), we found it advantageous to derive aperture corrections for point-source photometry from the images themselves using the same photometric software package. We used the same bright ($W1 < 15$ Vega mag) objects selected from the AllWISE catalogs used for the construction of the PRF (see Section 3.4). We then photometered those objects in the IRAC images using SExtractor with the same parameters as the source catalog (see Section 4 and Table 3), using the AllWISE point sources as an associated list with a search radius of 5 pixels ($4''$). SExtractor photometered these sources with circular apertures ranging in radius from $1''$ to $12''$, where the $12''$-radius aperture "defines" the total aperture (see Section 3.4, above).

Figures 9 and 10 compare the total $R = 12''$ aperture magnitudes of the AllWISE stars in the IRAC 3.6 and 4.5 μm frames to measurements performed in smaller apertures. As is clear from the figures, there are offsets owing to light lost outside the smaller apertures. We measure aperture corrections based on the median $m(<R) - m(<12'')$ magnitude for stars with magnitudes between 13.5 and 16 (AB) mag. (These median offsets are denoted by the long-dashed red lines in the figures.) At brighter magnitudes, $\lesssim 14$ mag, the effects of saturation cause the offsets to increase sharply, and become function of magnitude. We caution against using small aperture magnitudes in this regime, as they are unreliable.

Figure 11 shows the aperture corrections for the IRAC 3.6 and 4.5 μm data measured for point sources with magnitude between 13.5 and 16 mag in circular apertures, assuming an $R = 12''$ aperture encompasses the total light of a point source. Table 2 lists the aperture corrections. Our measurements are consistent with those of the IRAC Instrument Handbook (see footnote 21) and those derived in the literature (e.g., Ashby et al. 2009, 2013a) with differences at the <0.05 mag level. These differences likely depend on the method of photometry. We advocate the use of the aperture corrections derived here as they use the same photometric parameters as the source catalog. These corrections are accurate to better than 0.03 mag based on our comparison of the IRAC photometry to flux measurements from AllWISE at $W1$ (3.4 μm) and $W2$ (4.6 μm) in Section 3.6, below.

3.6. Photometric Quality: Comparison between SHELA IRAC and AllWISE

A test of the photometric accuracy of the SHELA IRAC data is possible by comparing the IRAC photometry to that measured by *WISE* at 3.4 μm ($W1$) and 4.6 μm ($W2$). For this test, we use the same point sources selected from the AllWISE catalog matched to the IRAC data discussed in Section 3.5, above, while applying an additional color cut, $-0.1 \leqslant [3.6]_{\rm Vega} - [4.5]_{\rm Vega} \leqslant 0.0$ to minimize potential color terms in the stellar atmospheres.[26] Figure 12 shows the magnitude difference between the IRAC [3.6] and *WISE* $W1$ photometry and between IRAC [4.5] and *WISE* $W2$

[26] See http://wise2.ipac.caltech.edu/docs/release/allwise/expsup/sec2_3a.html

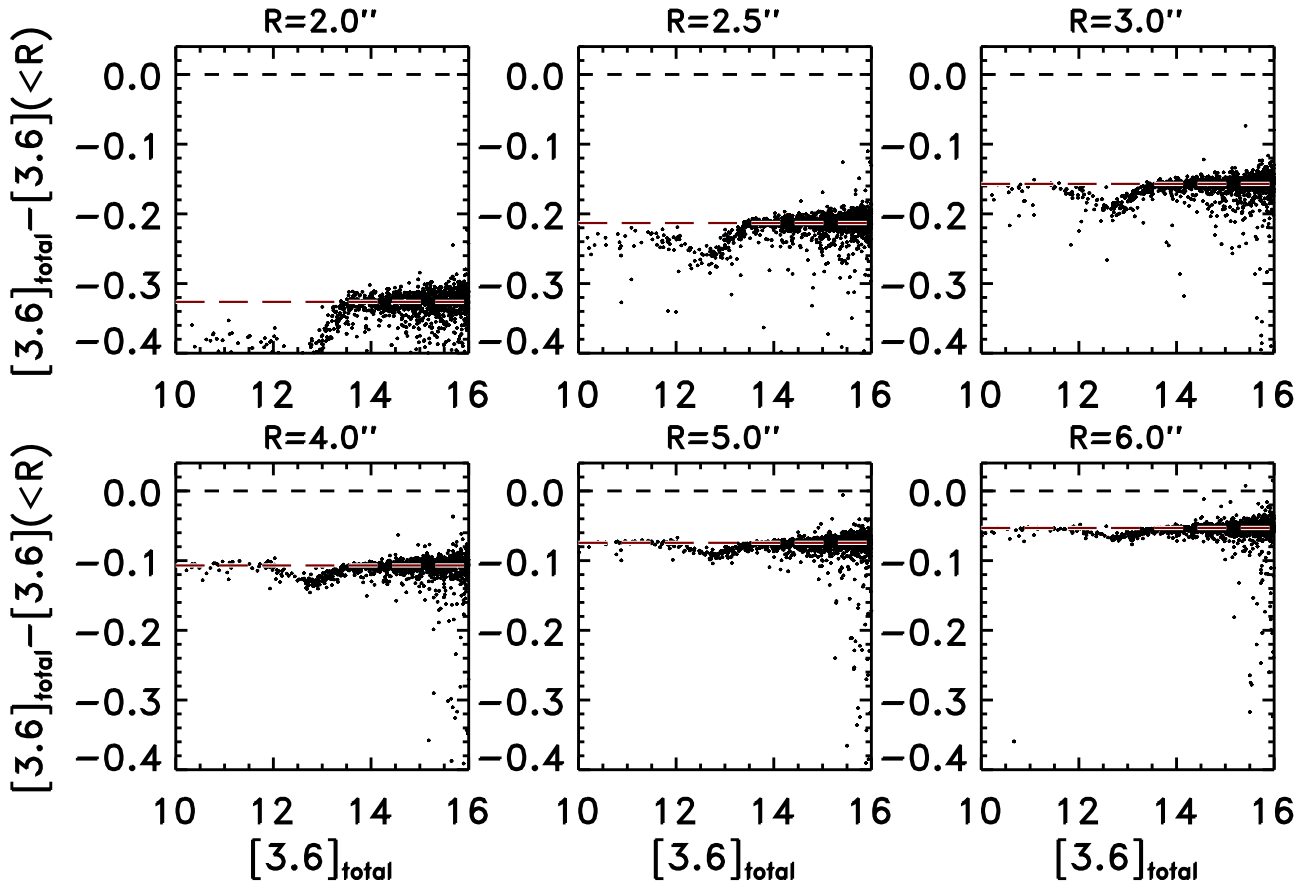

Figure 9. Estimate of light lost outside circular apertures of varying radius in the SHELA IRAC 3.6 μm image. Each panel shows the difference between a total magnitude (defined in a 12″-radius aperture) and the magnitude measured in a smaller circular aperture of radius R for point sources from the AllWISE catalog. Each panel shows a different aperture radius R, given above each panel. The dashed, thick red line in each panel shows the median difference for stars between $13.5 < [3.6] < 16$ mag, used to derive the aperture correction.

photometry. The AllWISE $W1$ and $W2$ catalogs have 5σ sensitivity limits $\gtrsim$16 mag (Vega, Cutri et al. 2013) so our comparison is for stars well above this limit and biases should be minimal. The difference between $[3.6] - W1$ is negligible. The figure shows this distribution, and a Gaussian fit, which gives a mean $\mu = 0.001$ mag and standard deviation, $\sigma = 0.023$ mag.

Figure 12 shows the distribution of $[4.5] - W2$, where a Gaussian fit gives a mean of $\mu = -0.028$ mag with $\sigma = 0.021$ mag. While this offset is small (-0.028 mag), its origin is unclear. The offset is 1.4σ times the scatter, and corresponds to a flux ratio of 1.8%. Jarrett et al. (2011) find similar offsets and conclude these are consistent with the differences in the IRAC and *WISE* bandpasses (the "relative system response" curves), and the uncertainty in the calibration. A similar offset is found by Cutri et al. (2013) between $W2 - [4.5]$ (see footnote 26) This offset persists regardless of the size of the photometric aperture (once corrected to total), so a systematic offset in the aperture correction seems unlikely. It therefore seems to be consistent with differences in the *WISE* $W2$ and IRAC [4.5] spectral response curves.

We furthermore considered (and rejected) the possibility that there are additional color terms between the IRAC and *WISE* photometry. Figure 13 shows the expected color between the IRAC and *WISE* bands for different stellar types, using models from Kurucz (1993) over a range of luminosity class and spectral type. The IRAC–*WISE* colors are zero (relative to Vega) for early-type (i.e., Vega-analogs) main-sequence stars. This is expected as these stars are used for the calibration of the instruments. However, the IRAC and *WISE* filters have different central wavelengths and filter widths. Therefore, there will be color terms depending on the source spectral energy distributions between the IRAC and *WISE* bands. These color terms include color-dependent transformations from the Vega to AB magnitude system. Nominally, the *WISE* AB-to-Vega system conversion constants are $W1_{\rm AB} - W1_{\rm Vega} = 2.699$ and $W2_{\rm AB} - W2_{\rm Vega} = 3.338$ (Jarrett et al. 2011). When compared to the conversions for IRAC, this implies an IRAC–*WISE* color offset of ~0.1 mag for Vega-like stars on the AB system (see also Richards et al. 2015).

Furthermore, because the *WISE* bands are broader in wavelength than the IRAC bands, they are more sensitive to the molecular absorption in later-type stellar atmospheres (e.g., H_2O, HCN, C_2H_2, CO), especially in the red giants, whose contribution to the SHELA field star counts may be substantial. As illustrated in Figure 13 late-type supergiants should have a IRAC–*Wise* photometric offset of of $[4.5] - W2 \approx -0.02$ mag, a value consistent with that observed in the data and that given in the literature (e.g., Jarrett et al. 2011). The offset between $[3.6] - W1$ is similarly small, though the fact that the bandpass contains of very different set of absorption features—H_2O, C_2H_2+HCN bands at 3.8 μm as opposed to CO bands at 5.0 μm (see Matsuura et al. 2005, 2014)—calls this interpretation into question. Therefore, while the color terms likely can explain the *scatter* in the IRAC–AllWISE colors (Figure 12), they likely are not the cause of the systematic offset between

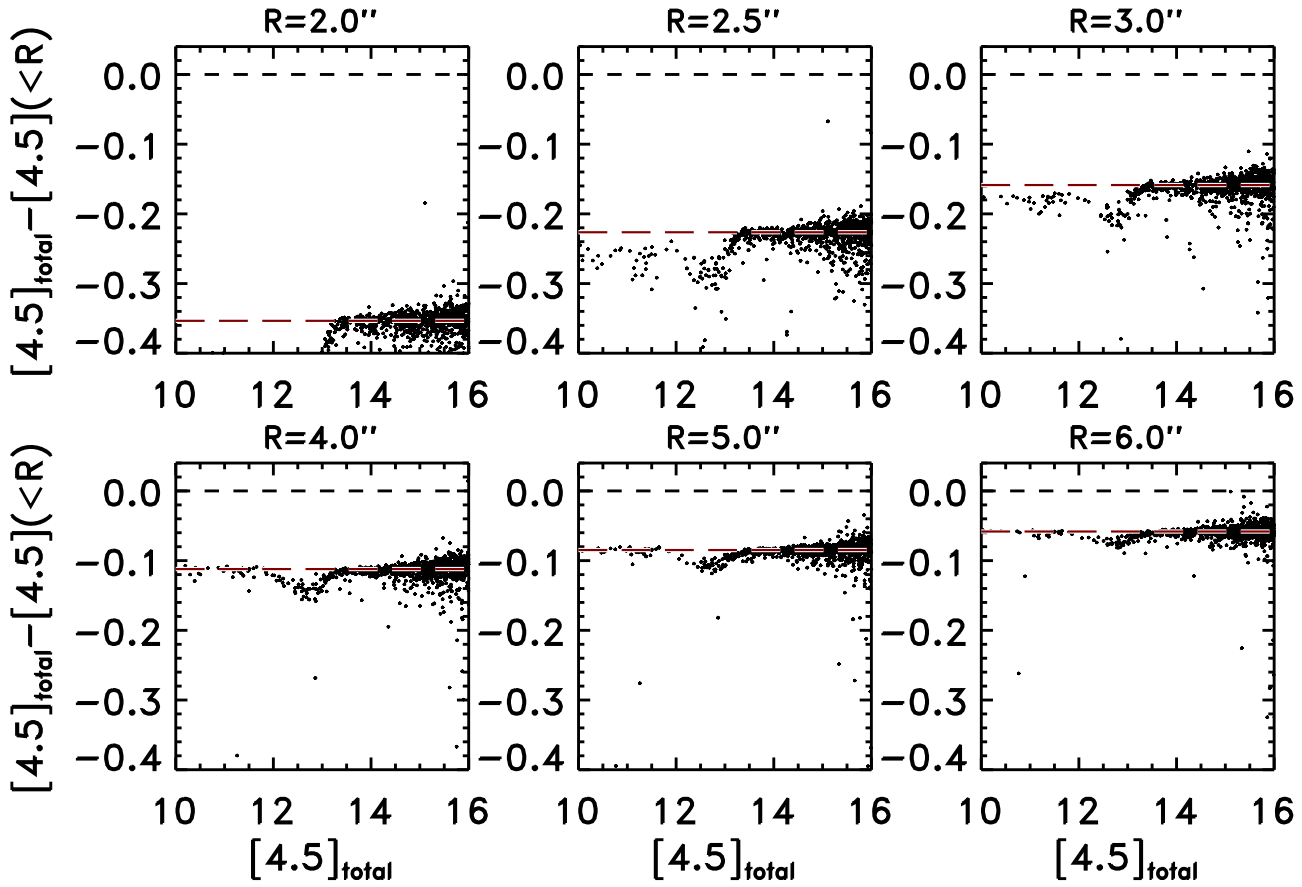

Figure 10. Same as Figure 9 for the SHELA IRAC 4.5 μm image.

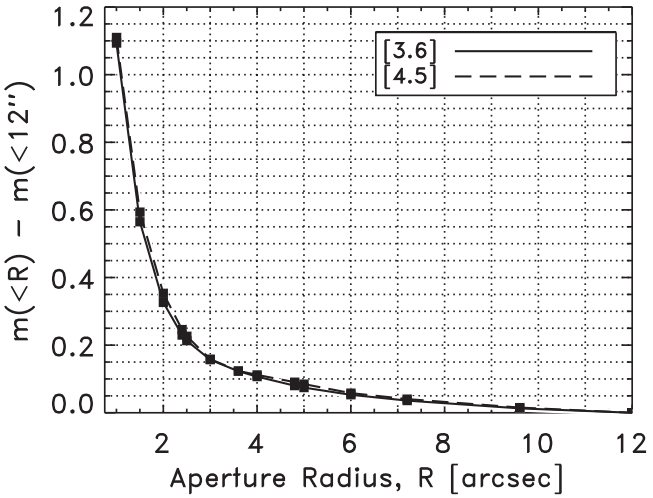

Figure 11. Aperture corrections for the IRAC images. The plot shows the difference between the IRAC photometric magnitude measured for point sources with magnitude between 13.5 and 16 mag in circular apertures of radius R and a total magnitude measured in an $R = 12''$ aperture. The aperture corrections are measured in apertures with discrete radii, as indicated by the solid black squares, and interpolated linearly between those points. The solid (dashed) line shows the 3.6 μm (4.5 μm) data, as labeled in the plot legend.

Table 2
Aperture Corrections for IRAC Data

R (pix) (1)	R (arcseconds) (2)	[3.6](<R) − [3.6](<12) (mag) (3)	[4.5](<R) − [4.5](<12) (mag) (4)
2.500	2.0	0.326	0.353
3.125	2.5	0.213	0.226
3.750	3.0	0.157	0.159
5.000	4.0	0.107	0.112
6.250	5.0	0.074	0.085
7.500	6.0	0.053	0.058

Note. The aperture correction is the difference between the magnitude measured in a circular aperture of radius R and the magnitude measured in a circular aperture of radius $12''$.

the IRAC 4.5 μm and AllWISE 4.6 μm photometry discussed above.

Regardless of its origin, the offset is small, and is within the uncertainty of the absolute IRAC calibration (Reach et al. 2005). Jarrett et al. (2011) argue the offset likely results from a combination of absolute calibrations, aperture corrections, and/or color corrections. The photometry is sufficiently accurate for most science applications, although those requiring better than 2% absolute photometric accuracy should be aware of this systematic.

4. SHELA IRAC CATALOGS

We used Source Extractor (SExtractor v. 2.19.5; Bertin & Arnouts 1996) to detect and to photometer sources in the IRAC images. To detect sources, we constructed a detection image as

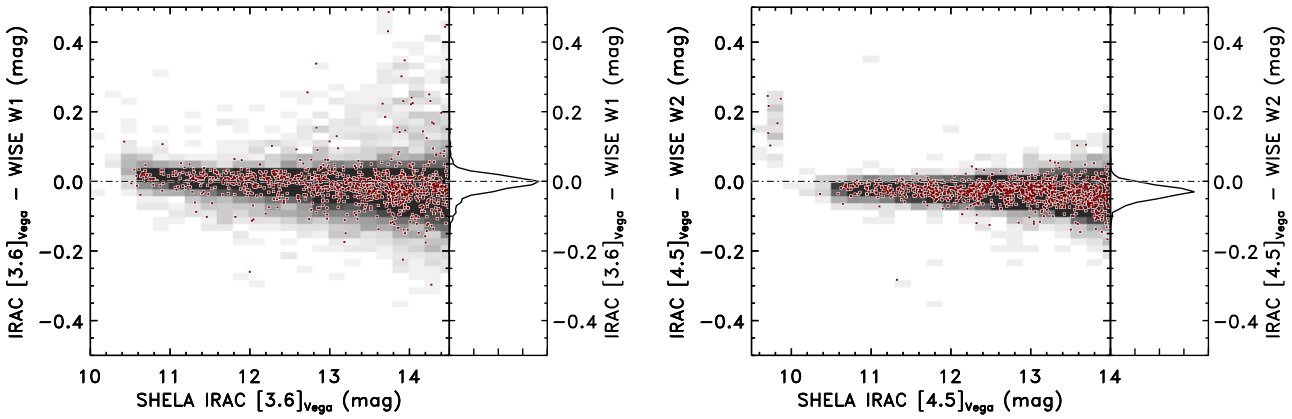

Figure 12. Magnitudes measured for point sources in the AllWISE catalog at 3.4 μm (*W*1) and 4.6 μm (*W*2) compared with those in the SHELA IRAC 3.6 and 4.5 μm data. Note that in this plot all magnitudes are relative to Vega-type stars. In both plots the gray shading shows all point sources, where darker regions correspond to a higher density of points falling in that region. The red points show a random subsample of the data. In each plot, the right panel shows the distribution of the magnitude difference between the IRAC and *WISE* image. The left plot compares the IRAC 3.6 μm and *WISE* W1 data. The photometric offset is negligible. The right plot compares the IRAC 4.5 μm and *WISE W*2 data. There is a small offset, −0.028 mag. Stars brighter than $\lesssim$10 (11) Vega mag appear saturated in the IRAC 3.6 (4.5) μm data.

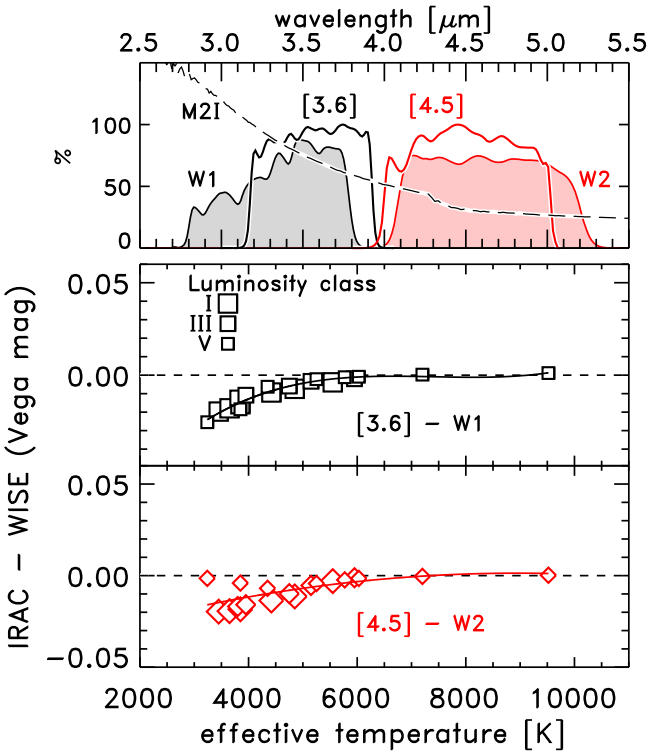

Figure 13. Expected differences between the IRAC and *WISE* photometry due to color variations in stars of different spectral types. The top panel compares the transmittance of the IRAC [3.6] and [4.5] filters to the *WISE W*1 and *W*2 filters, as labeled. The dashed line shows the spectrum of an M2I stellar template (Kurucz 1993). The bottom panels show synthesized colors between IRAC 3.6 μm and *WISE W*1, and between IRAC 4.5 μm and *WISE W*2, as labeled. The data points correspond to Kurucz (1993) models for dwarfs (luminosity class V), giants (class III), and supergiants (class I) over a range of effective temperature (spectral type). Because the *WISE* instrumental filters are wider, they can include bandhead absorption features in late-type stars, affecting the IRAC–*WISE* color up to 0.03 mag.

the weighted sum of the 3.6 and 4.5 μm images. The detection image, D, is then,

$$D = \frac{W_1 \times I_1 + W_2 \times I_2}{W_1 + W_2}, \quad (1)$$

Table 3
SHELA SExtractor Parameter Settings

SExtractor Parameter (1)	Value (2)
DETECT_MINAREA	3 pixels
DETECT_THRESH	1.5
ANALYSIS_THRESH	1.5
FILTER_NAME	Gauss_2.0_5 × 5[a]
WEIGHT_TYPE	MAP_WEIGHT
DEBLEND_NTHRESH	64
DEBLEND_MINCONT	0.0005
MAG_ZEROPOINT	20.9555[b]
PIXEL_SCALE	0.80 arcsec
BACK_TYPE	AUTO
BACK_SIZE	256 pixels
SEEING_FWHM	1.7 arcsec

Notes. SExtractor was run using the weighted sum of the 3.6 and 4.5 μm images for detection, and using the images separately for photometry. All SExtractor parameters are identical for both images. All other SExtractor parameters are set to the program defaults (for SExtractor v.2.19.5).
[a] This is a Gaussian kernel with $\sigma = 2$ pixels and size 5 × 5 pixel^2 used to filter the image for source detection.
[b] The AB magnitude zeropoint for the images, converting from the *Spitzer* default of MJy sr^{-1} to μJy pixel^{-1} at the 0.″8 pixel^{-1} scale.

where W_1 and W_2 are the weight maps (proportional to the exposure time) for the IRAC channel 1 and 2 images, respectively, and I_1 and I_2 are the science (flux) images for channel 1 and 2, respectively. We then ran SExtractor in "double image mode" using the detection image and science images with the parameters listed in Table 3. Tables 7 and 8 provide all the information from the full-mosaic catalogs.

We also constructed catalogs for the mosaics from each of the three observing epochs individually. For each epoch, we used the detection image for the combined images (see Equation (1) above). In this way, sources detected in the combined epoch, 3.6 + 4.5 μm image are photometered in each image from each epoch. We used the identical SExtractor parameters as for the full-mosaic catalogs (Table 3). Tables 9–11 provide the photometry from the individual epoch data.

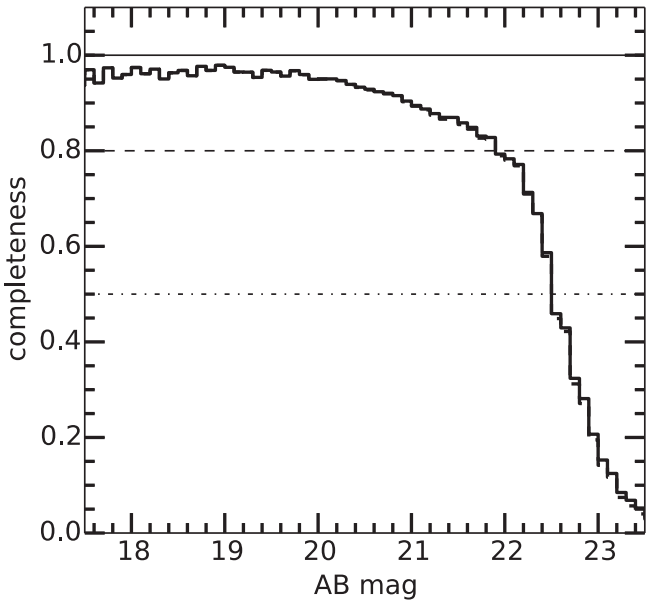

Figure 14. Completeness for point-sources in the SHELA data as a function of the input source magnitude. The plot shows the recovery fraction as a function of magnitude for simulated point sources, which are added to both the 3.6 and 4.5 μm images with the same AB magnitude. The solid-line histogram shows the raw completeness fraction. The dashed-line histogram shows the completeness corrected for "false positives" (sources that are "recovered" in the image, in which no simulated sources are added), which shows only slight differences with respect to the raw completeness fraction. The solid, dashed, and dotted–dashed horizontal lines show 100%, 80%, and 50% completeness.

4.1. Completeness Simulations

We performed simulations to estimate the completeness in the SHELA IRAC catalogs following the method in Papovich et al. (2015). We inserted fake point sources into the 3.6 and 4.5 images using the empirical PRFs derived above (Section 3.4). We inserted each fake source at the same (α, δ) location in the 3.6 and 4.5 μm images, where the source has the same total brightness (AB magnitude) in each channel. Fake sources were assigned magnitudes chosen randomly from a wide distribution (17–24th magnitude), and the sources are located randomly in the images. In this way fake sources may fall within the isophotes of real objects in the image, and therefore our completeness simulations include the effects from blended objects. We reconstructed the detection image as the weighted sum of the 3.6 and 4.5 μm images and reran SExtractor. This latter step was computationally expensive given the size of the images (see above; Equation (1)). We repeated the simulation only 15 times, where we inserted into each simulated image 10,000 fake sources (≈0.4% the total number of real sources). In this way we sampled the full range of source magnitude using a minimum investment of resources.

We computed the completeness as the ratio of the number of recovered (detected) fake sources to the number of input fake sources in bins of source magnitude. Figure 14 shows the completeness, where the 50% (80%) completeness limit is 22.6 (22.0) AB mag. Table 4 gives these as the "raw" completeness as a function of source magnitude in the detection image. We also added to the completeness a correction for "false positives," sources at the location of the fake that are "recovered" even when no sources are added to the image. Table 4 gives these as the "completeness." As illustrated in Figure 15 the difference between the raw completeness and the completeness corrected for false positives is small, accounting for only 1% of recovered sources down to the 50% completeness limit.

Table 4
Completeness and Error Estimates for SHELA IRAC Data

AB mag (1)	Raw Completeness (2)	Completeness (3)	$\sigma_{3.6}$ (4)	$\sigma_{4.5}$ (5)
18.0	0.98	0.98	0.02	0.02
18.5	0.97	0.97	0.02	0.02
19.0	0.98	0.98	0.02	0.02
19.5	0.97	0.97	0.03	0.03
20.0	0.95	0.95	0.05	0.05
20.5	0.94	0.94	0.07	0.07
21.0	0.90	0.90	0.11	0.12
21.5	0.86	0.86	0.17	0.17
22.0	0.79	0.79	0.25	0.25
22.5	0.57	0.56	0.37	0.38
23.0	0.20	0.19	0.49	0.51
23.5	0.05	0.04	0.76	0.77
24.0	0.01	0.00	0.90	0.87

Note. (1) Magnitude bin, (2) ratio of the number of recovered fake sources to the total number of fake sources in this magnitude bin, (3) completeness corrected for "false positives," fake sources recovered in the detection image even when no fake sources were added, (4) estimate of the photometric uncertainty for point sources in [3.6], (5) estimate of the photometric uncertainty for point sources in [4.5]. The photometric uncertainty estimates are the standard deviation between the input magnitudes and the measured magnitudes (measured in 2″-radii [i.e., 4″-diameter] apertures, corrected to total using the values in Table 2).

4.2. Error Estimates

We estimate uncertainties for sources in the IRAC catalogs using two methods. We first used the simulations from Section 4.1 to estimate the uncertainty for point sources of a given magnitude. In each of the IRAC 3.6 and 4.5 μm images, we computed the difference between the input ("true") magnitude and measured magnitude from SExtractor in $R = 2''$ radii (corrected to total using the aperture corrections in Table 2). Figure 15 shows the median and inter-68-percentile of the distributions of these differences as a function of [3.6] and [4.5] magnitude. The mean offset is near zero down to ≈22.2 mag (below the 80% completeness limit). In each bin of magnitude, we compute the ratio σ/F_ν (the inverse of the S/N) as a measure of the relative error for sources of that magnitude. The solid black line of Figure 16 shows this ratio as a function of [3.6] and [4.5]. This yields a limiting S/N = 5 at 22.0 AB mag, or a 1σ limit of 1.1 μJy for both [3.6] and [4.5].

This 1σ flux-density limit is consistent with estimates from the *Spitzer* SENS-PET for fields with higher background. SENS-PET gives for the "warm" *Spitzer* mission a 1σ limit for point sources of 0.9–1.2 μJy and 1.1–1.6 μJy for 3.6 and 4.5 μm observations for "medium" and "high" background (where as noted above, the medium and highs backgrounds in SENS-PET assume a sightline with latitude $\beta = 40°$ and 0° from the Ecliptic); therefore the values we derive are reasonable.

Figure 16 shows a "kink" in the error estimated from the simulations for both [3.6] and [4.5] below ≳22.5 mag (black, solid-lined curves in each panel of the figure). This is likely a bias owing to incompleteness of recovered sources. The 50 and 80% completeness limits are 22.6 and 22.0 mag, respectively.

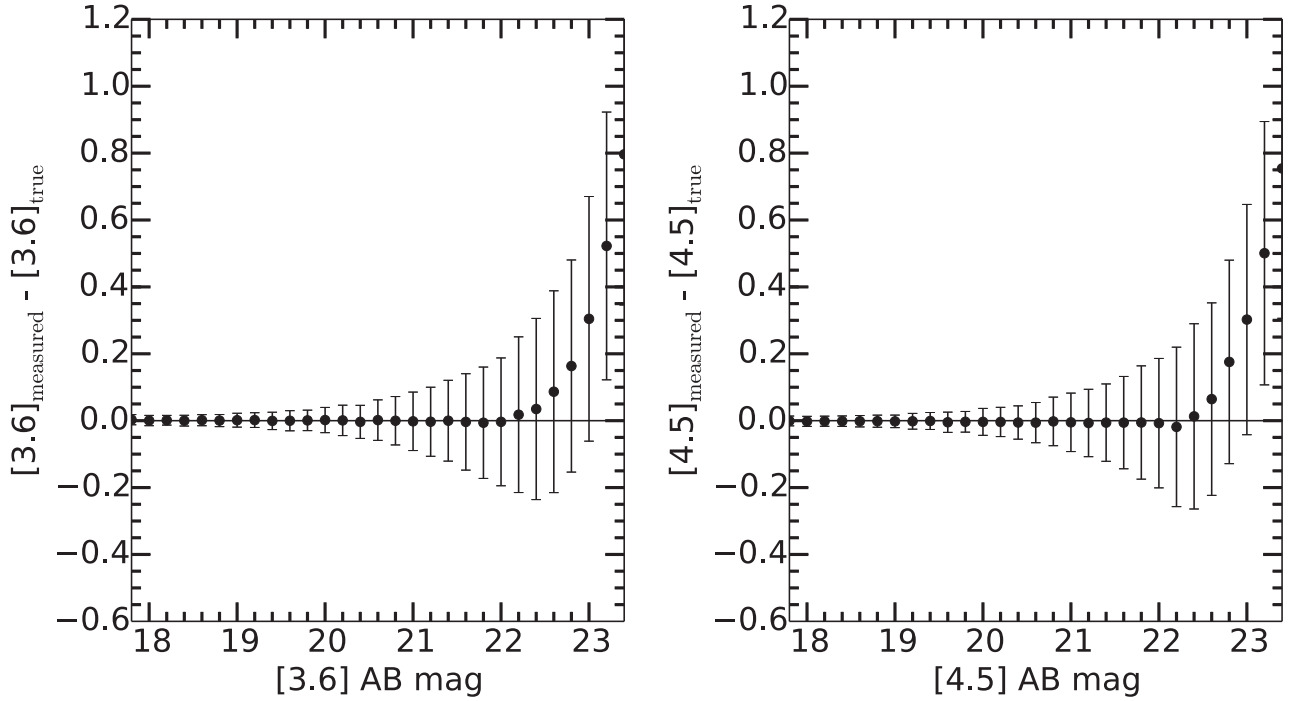

Figure 15. Comparison between the "true" (input) magnitude for simulated sources and the measured magnitude as a function of sources magnitude. The left panel shows the results for 3.6 μm, the right panel shows the results for 4.5 μm.

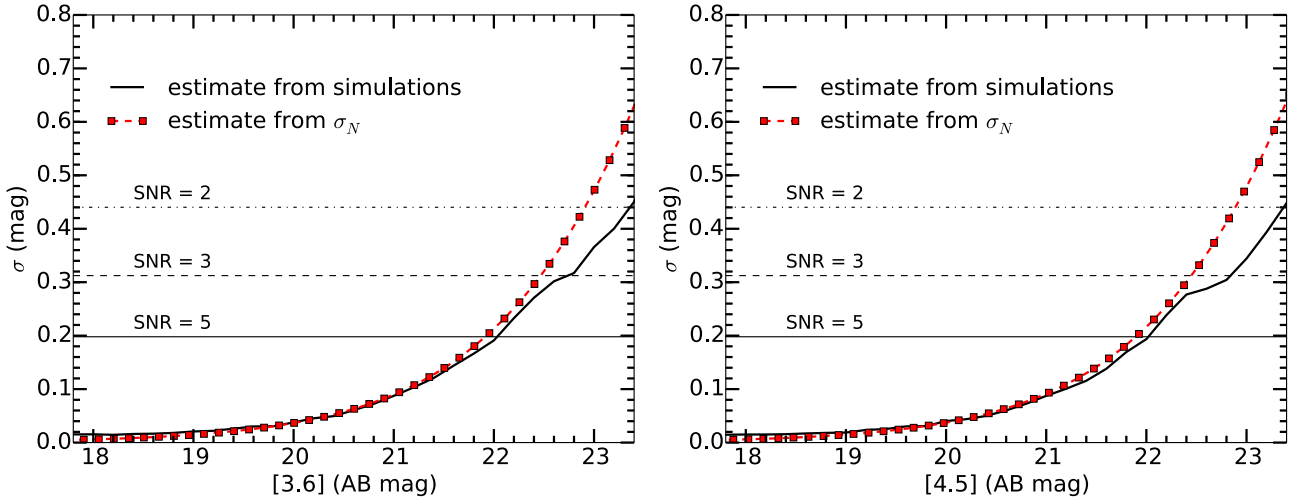

Figure 16. Estimates of uncertainties for the SHELA IRAC data. The left panel shows the results for the IRAC 3.6 μm data. The right panel shows the results for the 4.5 μm data. In each panel, the solid-line curve shows the estimated uncertainty measured from a comparison of the recovered magnitudes to the input magnitudes for fake sources added to the images. The points connected by the dashed-line curve show the estimates derived from σ_N for 2″-radii apertures, scaled to total magnitudes. The horizontal lines show the equivalent magnitude uncertainty for a source with S/N = 5, 3, and 2, as labeled.

Figure 15 shows that in this magnitude range, the median difference between recovered and input photometry is biased to positive values because fainter sources are missed in the catalog. Therefore, at these magnitudes, the distribution is clipped, and the inter-68 percentile range is biased smaller. This means the errors estimated from the simulations underestimate the true photometric uncertainty for sources with magnitudes below about the 80% completeness limit. Partly for this reason we will adopt the alternative method to estimate errors, described in the rest of this subsection below.

Second, we derived error estimates from the noise in the images in apertures of increasing number of pixels, N, where $N \propto A$, the area of the photometric aperture. The flux uncertainty within an aperture has a contribution from photon statistics. The theoretical uncertainty in an aperture with N pixels would then scale as $\sigma_N = \sigma_1 \times \sqrt{N}$, where σ_1 is the standard deviation of background pixels. This relation assumes that the pixel values are independent (uncorrelated). In practice, multiple effects are expected to introduce some pixel-to-pixel correlation, such as image alignment and mosaicking, sky subtraction, the extended wings of bright sources, and the flux from undetected objects. The limiting case of perfect correlations between pixels implies that the uncertainty in an aperture of N pixels should scale as $\sigma_N = \sigma_1 \times N$ (Quadri et al. 2007). Generalizing, we expect the uncertainty to scale with N^β with $0.5 < \beta < 1$, between the limiting cases of uncorrelated pixels

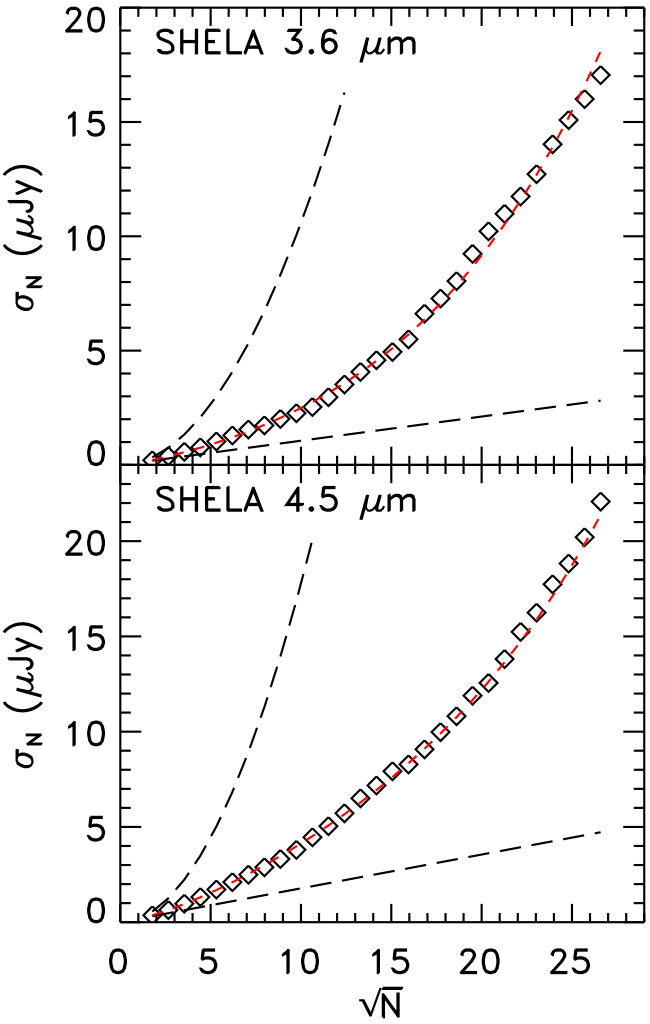

Figure 17. Scaling relation between the measured noise in the SHELA IRAC images and the square root of the number of pixels, $\sqrt{N}$, in the area of the photometric aperture. Both panels show the measured noise, σ_N, in each aperture of N pixels. The top panel shows the 3.6 μm data and the bottom panel shows the 4.5 μm data. In each panel, the bottom-most dashed line shows the theoretical relation assuming uncorrelated pixels in the Gaussian limit, $\sigma_N \sim \sqrt{N}$. The top-most dashed line shows the relation for perfectly correlated pixels ($\sigma_N \sim N$, Quadri et al. 2007). The red, short-dashed line shows the parameterized fit to the data, which we use to define the flux uncertainties measured in different-sized apertures.

and perfectly correlated pixels (see also Labbé et al. 2003; Gawiser et al. 2006; Blanc et al. 2008; Whitaker et al. 2011).

We estimated the noise as a function of pixels by measuring the sky counts in circular apertures of varying size in ≈5000 randomly placed regions in the SHELA IRAC images, ensuring that apertures do not overlap, and excluding regions containing objects. We then computed the standard deviation of the distribution of aperture fluxes from the normalized median absolute deviation, $\sigma_{\rm nmad}$ (Beers et al. 1990), as an estimate for σ_N for each aperture with N pixels. Figure 17 shows the measured relation of σ_N as a function of $\sqrt{N}$ for the 3-epoch IRAC [3.6] and [4.5] images.

Following the suggestion in Labbé et al. (2003), we fit a parameterized function to estimate the noise in an arbitrary aperture of linear size N,

$$\sigma_N = \sigma_1 (\alpha N^{\beta} + \gamma N^{\delta}), \quad (2)$$

Table 5
Coefficients for Error Estimates Using σ_N

Channel (1)	Epoch (2)	σ_1/μJy (3)	α (4)	β (5)	γ (6)	δ (7)
3.6 μm	Combined 3 Epochs	0.106	0.959	0.67	8.80×10^{-4}	1.77
	Single Epoch	0.178	0.944	0.69	1.98×10^{-3}	1.88
4.5 μm	Combined 3 Epochs	0.103	0.981	0.67	3.49×10^{-4}	2.28
	Single Epoch	0.169	0.893	0.70	1.95×10^{-6}	2.59

where σ_1 is the pixel-to-pixel standard deviation in the sky background, and α, β, γ, and δ are free parameters. We required that α and γ be non-negative, that $0.5 < \beta < 1$, and we placed no restrictions on δ. In this way the first term of Equation (2) represents the expected noise for partially correlated pixels. The second term includes an additional correction that better reproduces the noise in large apertures (see also, Labbé et al. 2003). Table 5 lists the parameters for the fits in Equation (2) for the combined, 3 epoch IRAC 3.6 and 4.5 μm data. The table also includes fits for the individual IRAC epoch data (where our tests showed each individual epoch had noise properties consistent with being the same, so we combined the random apertures of all individual images for a single fit).

The product of σ_1 α reflects the pixel-to-pixel rms, and these decrease roughly with the square-root of the exposure time such that the value of σ_1 for the 3-epoch combined image is roughly $\sqrt{3}$ lower than that for an individual epoch. The fitted values for the slope in the first term, $\beta \sim 0.6$–0.7, are consistent with partially correlated pixels, as found in other imaging surveys (e.g., Gawiser et al. 2006; Quadri et al. 2007). The values for γ are relatively small (the ratio of the coefficients is $\alpha/\gamma \sim 5 \times 10^2$–$5 \times 10^5$), implying there is a small, but increasing correction to the noise model for apertures with larger numbers of pixels.

The red points in Figure 16 show the magnitude uncertainty calculated for 2″-radius apertures (scaled up to the total aperture) as a function of [3.6] and [4.5]. There is generally good agreement between the estimated uncertainties from σ_N and those from the simulations described above. For objects with <22 AB mag, there is a slight offset, where the estimates from σ_N are lower at about the 0.02 mag level compared to the estimates from the completeness simulations. This could arise from several effects, including the fact that the completeness simulations allow fake objects to fall on image regions that contain other (real) galaxies. As this will tend to increase the average difference between the input and recovered magnitude, an offset is not unexpected. We include an additional 0.02 mag systematic uncertainty into our estimates to account for this effect (see below).

For the IRAC catalogs, we computed errors using Equation (2) for the number of pixels N in the aperture used to measure the object, scaled up to the total aperture. We add these errors in quadrature with an additional error $\sigma_{\rm sys} = 0.02$ mag, to account for systematics derived from the completeness simulations (see Section 4.1 and Table 2). The total

Table 6
Column Definitions in SHELA IRAC Catalog

Catalog Column Name[a]	Table Column Name[b]	Description	Units	Data Type
ID	…	Unique ID number from SExtractor for each source in the IRAC catalogs	…	long int
X[c]	…	x-pixel coordinate in IRAC image	pixel	float
Y[d]	…	y-pixel coordinate in IRAC images	pixel	float
R.A.	R.A.(J2000)	Right Ascension (J2000) of IRAC source	deg	double
decl.	decl.(J2000)	Declination (J2000) of IRAC source	deg	double
ISOAREA	Isophotal Area	isophotal area of source in detection image	arcsec^2	float
A	a	source semimajor axis	arcsec	float
E	e	source ellipticity, $e = 1 - b/a$, where b is the semiminor axis	…	float
THETA	θ	position angle of the semimajor axis, degrees east from celestial north	deg	float
W3P6	$W(3.6)$	value of the 3-epoch 3.6 μm weight map at the object's center position[e]	…	float
W4P5	$W(4.5)$	value of the 3-epoch 4.5 μm weight map at the object's center position[e]	…	float
W3P6_1	$W(3.6)_1$	value of the epoch 1, 3.6 μm weight map at the object's center position[e]	…	float
W4P5_1	$W(4.5)_1$	value of the epoch 1, 4.5 μm weight map at the object's center position[e]	…	float
W3P6_2	$W(3.6)_2$	value of the epoch 2, 3.6 μm weight map at the object's center position[e]	…	float
W4P5_2	$W(4.5)_2$	value of the epoch 2, 4.5 μm weight map at the object's center position[e]	…	float
W3P6_3	$W(3.6)_3$	value of the epoch 3, 3.6 μm weight map at the object's center position[e]	…	float
W4P5_3	$W(4.5)_3$	value of the epoch 3, 4.5 μm weight map at the object's center position[e]	…	float
FLAGS3P6	Flags (3.6 μm)	SExtractor flags for photometry of 3.6 μm image[f]	…	integer
FLAGS4P5	Flags (4.5 μm)	SExtractor flags for photometry of 4.5 μm image[f]	…	integer
F3P6_ISO	$f_{\nu,\mathrm{ISO}}^{(3.6)}$	Isophotal flux density for sources in the 3.6 μm image[f]	μJy	float
F3P6ERR_ISO	$\sigma_{\nu,\mathrm{ISO}}^{(3.6)}$	Error on the 3.6 μm isophotal flux density[f]	μJy	float
F4P5_ISO	$f_{\nu,\mathrm{ISO}}^{(4.5)}$	Isophotal flux density for sources in the 4.5 μm image[f]	μJy	float
F4P5ERR_ISO	$\sigma_{\nu,\mathrm{ISO}}^{(4.5)}$	Error on the 4.5 μm isophotal flux density[f]	μJy	float
F3P6_AUTO	$f_{\nu,AUTO}^{(3.6)}$	Total flux measured in the Kron aperture for sources in the 3.6 μm image[f]	μJy	float
F3P6ERR_AUTO	$\sigma_{\nu,AUTO}^{(3.6)}$	Error on the 3.6 μm total flux density[f]	μJy	float
F4P5_AUTO	$f_{\nu,AUTO}^{(4.5)}$	Total flux measured in a Kron aperture for sources in the 4.5 μm image[f]	μJy	float
F4P5ERR_AUTO	$\sigma_{\nu,AUTO}^{(4.5)}$	Error on the 4.5 μm total flux density[f]	μJy	float
F3P6_4ARCS	$f_{\nu,4''}^{(3.6)}$	Flux density measured at 3.6 μm for sources measured in 4″-diameter apertures[f,g]	μJy	float
F3P6ERR_4ARCS	$\sigma_{\nu,4''}^{(3.6)}$	Error on the flux density at 3.6 μm measured in the 4″-diameter apertures[f]	μJy	float
F4P5_4ARCS	$f_{\nu,4''}^{(4.5)}$	Flux density measured at 4.5 μm for sources measured in 4″-diameter apertures[f,g]	μJy	float
F4P5ERR_4ARCS	$\sigma_{\nu,4''}^{(4.5)}$	Error on the flux density at 4.5 μm measured in the 4″-diameter apertures[f]	μJy	float
F3P6_6ARCS	$f_{\nu,6''}^{(3.6)}$	Flux density measured at 3.6 μm for sources measured in 6″-diameter apertures[f,g]	μJy	float
F3P6ERR_6ARCS	$\sigma_{\nu,6''}^{(3.6)}$	Error on the flux density at 3.6 μm measured in the 6″-diameter apertures[f]	μJy	float
F4P5_6ARCS	$f_{\nu,6''}^{(4.5)}$	Flux density measured at 4.5 μm for sources measured in 6″-diameter apertures[f,g]	μJy	float
F4P5ERR_6ARCS	$\sigma_{\nu,6''}^{(4.5)}$	Error on the flux density at 4.5 μm measured in the 6″-diameter apertures[f]	μJy	float

Notes.
[a] Column name in binary FITS tables.
[b] Column name in Tables 7–11, if different from column name in binary FITS table.
[c] PIX_X in the catalog on IRSA.
[d] PIX_Y in the catalog on IRSA.
[e] The weight map values are proportional to the effective exposure time, with a constant of proportionality $t_{\mathrm{eff}} = 23.6$ s × Weight.
[f] These column names exist in each of the catalogs (combined 3 epoch, and individual epochs) with the same column names.
[g] The flux densities for sources measured in circular apertures have been corrected to total using the aperture corrections in Table 2.

photometric error, $\sigma_{i,c}$ on each source i in IRAC channel c is then given by

$$\sigma_{i,c}^2 = \frac{\sigma_{N,c}^2}{(w_{i,c}/w_{\mathrm{med},c})} + 0.921\ \sigma_{\mathrm{sys}} \times F_{i,c}, \quad (3)$$

where $F_{i,c}$ is the flux density of each object in each channel, $\sigma_{N,c}^2$ is given by Equation (2) for each channel, $w_{i,c}$ is the value of the weight map at the location of each object, and $w_{\mathrm{med},c}$ is the median value of the weight map in each channel. We opted to use these uncertainty estimates as they can be scaled to arbitrarily sized apertures (unlike the errors on the simulations, which are otherwise valid only for point sources).

4.3. Catalogs

With this paper, we publish the full SHELA photometric catalogs. The catalogs include the IRAC fluxes measured in multiple apertures (4″ and 6″ diameter circular apertures, corrected to total magnitudes, isophotal magnitudes, and the "total" (MAG_AUTO) magnitudes from SExtractor). Errors are estimated from Equation (2) and Table 5 for the number of pixels for each object/aperture. In addition, we include a catalog with photometry for the IRAC sources from the SDSS Stripe 82 coadd field (Annis et al. 2014) in $ugriz$, where sources in the SHELA catalog have been matched to the astrometric positions of sources in the SDSS Stripe 82 catalogs using a 1″ search radius. Only SDSS sources matched to

Table 7
Preamble for all SHELA IRAC Catalogs

ID	X (pixel)	Y (pixel)	R.A.(J2000) (deg)	decl.(J2000) (deg)	Isophotal Area (arcseconds^2)	a (arcseconds)	e	θ (deg)	$W(3.6)$	$W(4.5)$	$W(3.6)_1$	$W(4.5)_1$	$W(3.6)_2$	$W(4.5)_2$	$W(3.6)_3$	$W(4.5)_3$
(1)	(2)	(3)	(4)	(5)	(6)	(7)	(8)	(9)	(10)	(11)	(12)	(13)	(14)	(15)	(16)	(17)
100020	45386.8	1082.6	17.701277	−1.132968	125.4	1.9	0.04	35.3	2.92	6.03	0.00	1.02	2.92	3.00	0.00	2.00
100021	18859.7	1115.1	23.590947	−1.125582	7.0	0.8	0.25	−13.1	8.01	10.76	3.00	3.01	2.02	4.77	2.99	2.99
100022	19340.1	1112.4	23.484482	−1.126288	12.2	1.1	0.26	−0.7	6.32	6.03	3.28	2.99	0.00	0.00	3.04	3.05
100023	19528.0	1112.8	23.442827	−1.126232	12.2	1.1	0.46	−29.2	6.03	7.06	3.04	3.03	0.00	0.00	2.99	4.03
100024	56605.8	1102.2	15.221331	−1.125113	26.9	1.2	0.11	−53.5	4.08	9.01	0.00	2.98	4.08	3.03	0.00	3.01
100025	22941.5	1112.9	22.685727	−1.126878	7.0	0.8	0.31	−41.1	11.12	9.05	5.03	2.99	3.04	3.01	3.05	3.05
100026	21391.8	1115.2	23.029557	−1.126084	3.8	0.6	0.25	−47.4	3.04	6.79	0.00	2.77	3.04	0.00	0.00	4.01
100027	45127.6	1104.6	17.758739	−1.128140	25.6	1.3	0.14	−32.0	7.18	7.15	3.00	4.11	4.17	3.03	0.00	0.00
100028	28402.5	1118.5	21.473082	−1.126254	5.8	0.8	0.56	−18.8	2.99	6.15	0.00	3.14	2.99	0.00	0.00	3.01
100029	35643.7	1111.3	19.864062	−1.127908	12.2	1.0	0.19	−32.0	0.00	8.06	0.00	5.05	0.00	0.00	0.00	3.01
100030	22402.3	1098.1	22.805387	−1.130069	30.1	1.9	0.42	−65.9	8.00	9.09	3.02	3.11	2.99	2.99	1.99	2.99
100031	26946.7	1113.5	21.796466	−1.127243	6.4	0.8	0.30	−89.2	3.00	3.01	3.00	3.01	0.00	0.00	0.00	0.00
100032	8436.4	1095.7	25.894587	−1.126576	62.7	2.1	0.23	−7.7	9.07	6.03	6.03	2.98	0.00	0.00	3.04	3.05
100033	28542.3	1118.6	21.442033	−1.126240	3.2	0.6	0.39	−16.6	2.99	6.02	0.00	3.03	2.99	0.00	0.00	2.99
100034	27031.2	1113.5	21.777696	−1.127268	5.1	0.9	0.55	67.7	3.00	3.38	3.00	3.38	0.00	0.00	0.00	0.00
100035	29155.7	1118.3	21.305746	−1.126346	1.9	0.5	0.40	44.8	14.88	6.01	3.02	3.00	8.84	0.00	3.02	3.00
100036	41240.4	1091.2	18.621071	−1.131813	84.5	1.8	0.24	34.9	9.07	10.76	3.03	2.41	3.04	3.02	3.00	5.34
100037	33861.8	1108.3	20.259993	−1.128661	16.6	1.1	0.16	−23.1	9.04	8.14	3.03	2.11	2.99	2.99	3.02	3.04
100038	40805.0	1105.7	18.717715	−1.128666	21.8	1.1	0.14	59.5	7.94	4.25	3.03	2.03	2.88	0.00	2.02	2.22
100039	50844.3	1103.6	16.492991	−1.126869	21.1	1.5	0.43	−82.5	5.17	6.04	2.15	3.00	0.00	0.00	3.02	3.04
100040	34697.3	1108.7	20.074340	−1.128531	14.7	1.1	0.17	79.3	0.00	4.85	0.00	3.01	0.00	0.00	0.00	1.85
100041	35355.1	1108.5	19.928174	−1.128544	19.2	1.1	0.14	−62.1	0.00	6.08	0.00	3.06	0.00	0.00	0.00	3.02

Note. The full table is published in its entirety at http://irsa.ipac.caltech.edu/data/SPITZER/SHELA/catalogs. This is a portion of the full table to provide form and guidance. (1) Unique object ID number, (2) central X pixel coordinate, (3) central Y pixel coordinate, (4) object R.A. (J2000) in decimal degrees, (5) object decl. (J2000) in decimal degrees, (6) Isophotal area in the detection (combined 2 band, 3 epoch) image, (7) semimajor axis in the detection image, (8) ellipticity measured in the detection image, defined as $e = 1 - b/a$, where b and a are the semiminor and semimajor axes, respectively, (9) position angle measured in the detection image (degrees E from N), (10)–(17) values of the weight maps in the images at the location of the object. The weight map is proportional to the exposure time map. (10)–(11) Values in combined 3.6 and 4.5 μm image weight maps, respectively. (12)–(17) Values in the 3.6 and 4.5 μm weight maps for the individual epochs, respectively.

Table 8
Photometry for Combined, 3 Epoch SHELA IRAC Catalogs

ID	Flags (3.6μm)	Flags (4.5μm)	$f_{\nu,\mathrm{ISO}}^{(3.6)}$ (μJy)	$\sigma_{\mathrm{ISO}}^{(3.6)}$ (μJy)	$f_{\nu,\mathrm{AUTO}}^{(3.6)}$ (μJy)	$\sigma_{\mathrm{AUTO}}^{(3.6)}$ (μJy)	$f_{\nu,4''}^{(3.6)}$ (μJy)	$\sigma_{4''}^{(3.6)}$ (μJy)	$f_{\nu,6''}^{(3.6)}$ (μJy)	$\sigma_{6''}^{(3.6)}$ (μJy)	$f_{\nu,\mathrm{ISO}}^{(4.5)}$ (μJy)	$\sigma_{\mathrm{ISO}}^{(4.5)}$ (μJy)	$f_{\nu,\mathrm{AUTO}}^{(4.5)}$	$\sigma_{\mathrm{AUTO}}^{(4.5)}$ (μJy)	$f_{\nu,4''}^{(4.5)}$ (μJy)	$\sigma_{4''}^{(4.5)}$ (μJy)	$f_{\nu,6''}^{(4.5)}$ (μJy)	$\sigma_{6''}^{(4.5)}$ (μJy)
(1)	(2)	(3)	(4)	(5)	(6)	(7)	(8)	(9)	(10)	(11)	(12)	(13)	(14)	(15)	(16)	(17)	(18)	(19)
100020	2	2	454	8.34	452	8.73	334	2.81	408	3.61	525	6.27	525	6.52	392	2.84	470	3.37
100021	0	0	2.86	0.585	10.2	2.92	4.72	0.853	5.76	1.46	2.98	0.52	3.81	2.5	5.06	0.755	4.37	1.26
100022	2	2	5.7	0.939	6.89	3.51	7.33	0.973	8.93	1.65	5.09	0.952	8.42	3.59	6.96	0.989	7.03	1.67
100023	1	1	3.72	0.939	2.87	1.45	2.93	0.951	2.42	1.65	5.71	0.894	7.46	1.37	6.78	0.923	7.35	1.56
100024	0	0	43.5	2.12	45	3.11	48.5	1.47	49.3	2.21	26.7	1.47	26.8	2.12	31.5	1.07	30.8	1.54
100025	0	0	3.24	0.518	6.68	2.1	5.23	0.747	6.22	1.25	2.92	0.557	4.03	2.32	4.25	0.803	3.16	1.36
100026	0	0	2.05	0.612	3.47	1.16	4.99	1.33	4.78	2.32	2.47	0.443	3.54	0.798	4.7	0.918	3.96	1.57
100027	0	0	19	1.52	20	2.5	19.7	1.04	20.8	1.62	23.7	1.55	25.5	2.52	26.6	1.1	27	1.66
100028	0	0	1.68	0.788	1.9	1.93	3.78	1.34	3.73	2.34	3.36	0.591	4.2	1.37	4.68	0.959	4.35	1.64
100029	1	0	0	0	0	0	0	0	0	0	9.3	0.882	10.5	1.61	12.4	0.93	12.2	1.49
100030	3	3	17.9	1.59	19.5	3.16	13.7	0.946	18.1	1.53	13.3	1.48	12.8	2.95	9.71	0.862	12.9	1.42
100031	0	0	4.34	0.871	7.98	2.18	8.21	1.36	8.4	2.35	3.87	0.865	6.03	2.17	6.95	1.35	6.44	2.34
100032	3	3	70.5	2.7	73.3	4.63	56.7	1.27	62.9	1.71	79.8	3.24	80.6	5.63	65.3	1.43	71.4	2
100033	0	0	1.92	0.55	1.41	1.18	1.7	1.32	−2.2	2.32	1.7	0.405	4.35	0.871	5.35	0.975	4.69	1.66
100034	1	1	2.63	0.742	26.4	6.25	6.69	1.35	12.3	2.37	2.16	0.697	14.8	5.87	5.03	1.27	6.49	2.21
100035	0	0	0.65	0.198	1.29	0.88	2.3	0.622	1.57	1.06	0.932	0.29	1.7	1.37	2.19	0.946	0.553	1.64
100036	2	2	152	3.55	151	3.89	142	1.78	149	2.13	136	3.28	136	3.59	127	1.68	133	1.99
100037	3	3	7.04	0.984	7.71	3.35	8.53	0.851	8.55	1.39	7.45	1.03	10.9	3.54	9	0.892	11.1	1.48
100038	0	0	21.2	1.34	25.3	2.97	24.4	1.05	25.1	1.58	14.3	1.69	14.3	3.99	16.4	1.23	16.5	2.03
100039	2	2	13.4	1.52	14.9	4.49	12.9	1.11	15.3	1.84	12.9	1.41	17.3	4.16	11.8	1.03	16.9	1.73
100040	1	0	0	0	0	0	0	0	0	0	14.8	1.26	15.8	2.51	18.3	1.18	18.4	1.91
100041	1	0	0	0	0	0	0	0	0	0	23.9	1.4	26.4	0.697	28.5	1.17	28.8	1.78

Note. The full table is published in its entirety at http://irsa.ipac.caltech.edu/data/SPITZER/SHELA/catalogs. This is a portion of the full table to provide form and guidance. (1) Object ID number in Table 7, (2) SExtractor flags in the 3.6 μm image, (3) SExtractor flags in the 4.5 μm image, (4) isophotal flux in the 3.6 μm image, (5) error on isophotal flux, (6) total (Kron) flux in 3.6 μm image, (7) error on total flux, (8) 3.6 μm flux measured in 4″-diameter aperture, corrected to total, (9) error on 4″-diameter flux, 10. 3.6 μm flux measured in 6″-diameter aperture, corrected to total, (11) error on 6″-diameter flux, 12. isophotal flux in the 4.5 μm image, (13) error on isophotal flux, (14) total (Kron) flux in 4.5 μm image, (15) error on total flux, (16) 4.5 μm flux measured in 4″-diameter aperture, corrected to total, (17) error on 4″-diameter flux, (18) 4.5 μm flux measured in 6″-diameter aperture, corrected to total, (19) error on 6″-diameter flux.

Table 9
Photometry for SHELA Epoch 1 IRAC Catalogs

ID	Flags (3.6 μm)	Flags (4.5 μm)	$f_{\nu,\mathrm{ISO}}^{(3.6)}$ (μJy)	$\sigma_{\mathrm{ISO}}^{(3.6)}$ (μJy)	$f_{\nu,\mathrm{AUTO}}^{(3.6)}$ (μJy)	$\sigma_{\mathrm{AUTO}}^{(3.6)}$ (μJy)	$f_{\nu,4''}^{(3.6)}$ (μJy)	$\sigma_{4''}^{(3.6)}$ (μJy)	$f_{\nu,6''}^{(3.6)}$ (μJy)	$\sigma_{6''}^{(3.6)}$ (μJy)	$f_{\nu,\mathrm{ISO}}^{(4.5)}$ (μJy)	$\sigma_{\mathrm{ISO}}^{(4.5)}$ (μJy)	$f_{\nu,\mathrm{AUTO}}^{(4.5)}$	$\sigma_{\mathrm{AUTO}}^{(4.5)}$ (μJy)	$f_{\nu,4''}^{(4.5)}$ (μJy)	$\sigma_{4''}^{(4.5)}$ (μJy)	$f_{\nu,6''}^{(4.5)}$ (μJy)	$\sigma_{6''}^{(4.5)}$ (μJy)
(1)	(2)	(3)	(4)	(5)	(6)	(7)	(8)	(9)	(10)	(11)	(12)	(13)	(14)	(15)	(16)	(17)	(18)	(19)
100020	3	2	0	0	0	0	0	0	0	0	506	12.2	514	12.7	385	3.46	463	4.86
100021	0	0	3.78	0.904	9.91	4.45	6.02	1.33	5.85	2.29	2.46	0.889	−2.32	4.42	3.5	1.31	0.925	2.27
100022	2	2	8.11	1.27	9.44	4.54	10.6	1.31	13.4	2.23	4.43	1.29	10.2	4.76	5.82	1.33	5.77	2.3
100023	1	1	3.32	1.28	1.02	1.98	2.42	1.3	−0.875	2.25	5.19	1.29	6.8	2.01	5.91	1.32	5.83	2.28
100024	1	0	0	0	0	0	0	0	0	0	27.2	2.31	28.1	3.42	30.7	1.5	31.7	2.4
100025	0	0	2.4	0.7	3.13	2.95	3.14	1.02	3.39	1.77	3.04	0.898	5.76	3.82	5.29	1.33	4.44	2.29
100026	1	0	0	0	0	0	0	0	0	0	2.17	0.626	3.71	1.19	5.17	1.38	3.62	2.37
100027	0	0	22.4	2.21	26.4	3.65	22.5	1.44	25.4	2.37	24.2	1.93	26.3	3.14	26.6	1.3	27.5	2.06
100028	1	0	0	0	0	0	0	0	0	0	3.47	0.779	4.3	1.87	4.69	1.29	4.92	2.24
100029	1	0	0	0	0	0	0	0	0	0	9.98	1.06	13	1.96	13.4	1.11	13.9	1.82
100030	3	3	18.6	2.43	16.8	4.74	14.5	1.38	20.6	2.34	11.5	2.37	12.1	4.66	8.36	1.32	12.1	2.28
100031	0	0	4.28	0.857	7.92	2.14	8.11	1.35	8.37	2.3	3.75	0.849	5.89	2.13	6.7	1.33	6.27	2.29
100032	3	3	71.1	3.06	71.4	5.03	56.6	1.37	63.4	1.93	84.9	4.23	84.5	7.07	68.9	1.71	76	2.56
100033	1	0	0	0	0	0	0	0	0	0	0.851	0.516	2.37	1.16	2.18	1.3	0.543	2.26
100034	1	1	2.67	0.729	26	5.72	6.61	1.34	12.1	2.32	2.14	0.684	15.1	5.37	5.06	1.25	6.55	2.17
100035	0	0	0.233	0.36	−1.22	1.89	0.9	1.29	−0.846	2.26	1.01	0.38	2.14	1.9	2.5	1.31	1.23	2.27
100036	2	2	148	5.28	149	5.8	141	2.06	148	2.8	147	5.86	146	6.45	128	2.1	137	2.99
100037	3	3	5.01	1.59	3.26	5.31	5.99	1.33	6.37	2.28	9.81	1.92	17.8	6.38	11.1	1.6	17.4	2.77
100038	0	0	18	1.96	19.1	4.44	20.9	1.42	21.1	2.34	13.7	2.35	14	5.41	17.2	1.67	15.4	2.81
100039	2	2	15	2.25	19.5	6.39	14	1.6	15.6	2.73	12.6	1.91	22.5	5.42	10.2	1.36	15.1	2.33
100040	1	0	0	0	0	0	0	0	0	0	16.3	1.54	17.9	3.07	20.4	1.43	20.3	2.35
100041	1	0	0	0	0	0	0	0	0	0	22	1.83	24.2	0.668	26.4	1.45	27	2.35

Note. The full table is published in its entirety at http://irsa.ipac.caltech.edu/data/SPITZER/SHELA/catalogs. This is a portion of the full table to provide form and guidance. (1) Object ID number in Table 7, (2) SExtractor flags in the 3.6 μm image, (3) SExtractor flags in the 4.5 μm image, (4) isophotal flux in the 3.6 μm image, (5) error on isophotal flux, (6) total (Kron) flux in 3.6 μm image, (7) error on total flux, (8) 3.6 μm flux measured in 4″-diameter aperture, corrected to total, (9) error on 4″-diameter flux, (10) 3.6 μm flux measured in 6″-diameter aperture, corrected to total, (11) error on 6″-diameter flux, (12) isophotal flux in the 4.5 μm image, (13) error on isophotal flux, (14) total (Kron) flux in 4.5 μm image, (15) error on total flux, (16) 4.5 μm flux measured in 4″-diameter aperture, corrected to total, (17) error on 4″-diameter flux, (18) 4.5 μm flux measured in 6″-diameter aperture, corrected to total, (19) error on 6″-diameter flux.

Table 10
Photometry for SHELA Epoch 2 IRAC Catalogs

ID	Flags (3.6μm)	Flags (4.5μm)	$f_{\nu,\mathrm{ISO}}^{(3.6)}$ (μJy)	$\sigma_{\mathrm{ISO}}^{(3.6)}$ (μJy)	$f_{\nu,\mathrm{AUTO}}^{(3.6)}$ (μJy)	$\sigma_{\mathrm{AUTO}}^{(3.6)}$ (μJy)	$f_{\nu,4''}^{(3.6)}$ (μJy)	$\sigma_{4''}^{(3.6)}$ (μJy)	$f_{\nu,6''}^{(3.6)}$ (μJy)	$\sigma_{6''}^{(3.6)}$ (μJy)	$f_{\nu,\mathrm{ISO}}^{(4.5)}$ (μJy)	$\sigma_{\mathrm{ISO}}^{(4.5)}$ (μJy)	$f_{\nu,\mathrm{AUTO}}^{(4.5)}$	$\sigma_{\mathrm{AUTO}}^{(4.5)}$ (μJy)	$f_{\nu,4''}^{(4.5)}$ (μJy)	$\sigma_{4''}^{(4.5)}$ (μJy)	$f_{\nu,6''}^{(4.5)}$ (μJy)	$\sigma_{6''}^{(4.5)}$ (μJy)
(1)	(2)	(3)	(4)	(5)	(6)	(7)	(8)	(9)	(10)	(11)	(12)	(13)	(14)	(15)	(16)	(17)	(18)	(19)
100020	2	2	453	7.49	451	7.74	334	2.82	408	3.64	523	7.48	521	7.73	391	2.99	469	3.76
100021	0	0	1.05	1.07	11.7	5.56	3.25	1.63	6.56	2.89	4.23	0.747	7.81	3.62	7.25	1.11	6.32	1.9
100022	3	3	0	0	0	0	0	0	0	0	0	0	0	0	0	0	0	0
100023	1	1	0	0	0	0	0	0	0	0	0	0	0	0	0	0	0	0
100024	0	0	43.5	2.14	45.1	3.1	48.4	1.47	49.3	2.23	28.3	2.37	28.7	3.51	32.2	1.52	32.3	2.47
100025	0	0	4.27	0.913	1.29	3.91	6.68	1.36	4.18	2.36	4.44	0.919	9	3.95	6.81	1.37	6.67	2.38
100026	0	1	2.09	0.597	3.5	1.16	4.95	1.35	4.36	2.36	0	0	0	0	0	0	0	0
100027	0	0	16.8	1.94	15.8	3.19	17.9	1.26	17.8	2.08	22	2.27	22.8	3.74	25.6	1.48	24.8	2.44
100028	0	1	1.7	0.779	2.02	1.96	3.8	1.35	3.82	2.37	0	0	0	0	0	0	0	0
100029	1	1	0	0	0	0	0	0	0	0	0	0	0	0	0	0	0	0
100030	3	3	17.3	2.53	19.1	4.88	13.8	1.42	16.1	2.42	18.5	2.53	20	4.88	13.2	1.41	18.4	2.43
100031	1	1	0	0	0	0	0	0	0	0	0	0	0	0	0	0	0	0
100032	3	3	0	0	0	0	0	0	0	0	0	0	0	0	0	0	0	0
100033	0	1	1.9	0.533	1.42	1.19	1.72	1.33	−2.22	2.36	0	0	0	0	0	0	0	0
100034	1	1	0	0	0	0	0	0	0	0	0	0	0	0	0	0	0	0
100035	0	1	0.744	0.233	−0.221	1.14	1.39	0.786	−0.559	1.37	0	0	0	0	0	0	0	0
100036	2	2	146	5.36	145	5.85	139	2.07	146	2.86	125	5.34	124	5.83	126	2.01	129	2.81
100037	3	3	7.01	1.66	7.93	5.43	8.07	1.38	7.97	2.39	5.79	1.65	8.11	5.43	7.35	1.37	8.29	2.39
100038	0	1	22.7	2.1	30.6	4.7	26.6	1.52	27.2	2.5	0	0	0	0	0	0	0	0
100039	3	3	0	0	0	0	0	0	0	0	0	0	0	0	0	0	0	0
100040	1	1	0	0	0	0	0	0	0	0	0	0	0	0	0	0	0	0
100041	1	1	0	0	0	0	0	0	0	0	0	0	0	0	0	0	0	0

Note. The full table is published in its entirety at http://irsa.ipac.caltech.edu/data/SPITZER/SHELA/catalogs. This is a portion of the full table to provide form and guidance. (1) Object ID number in Table 7, (2) SExtractor flags in the 3.6 μm image, (3) SExtractor flags in the 4.5 μm image, (4) isophotal flux in the 3.6 μm image, (5) error on isophotal flux, (6) total (Kron) flux in 3.6 μm image, (7) error on total flux, (8) 3.6 μm flux measured in 4″-diameter aperture, corrected to total, (9) error on 4″-diameter flux, (10) 3.6 μm flux measured in 6″-diameter aperture, corrected to total, (11) error on 6″-diameter flux, (12) isophotal flux in the 4.5 μm image, (13) error on isophotal flux, (14) total (Kron) flux in 4.5 μm image, (15) error on total flux, 16. 4.5 μm flux measured in 4″-diameter aperture, corrected to total, (17) error on 4″-diameter flux, (18) 4.5 μm flux measured in 6″-diameter aperture, corrected to total, (19) error on 6″-diameter flux.

Table 11
Photometry from SHELA Epoch 3 IRAC Catalogs

ID	Flags (3.6μm)	Flags (4.5μm)	$f_{\nu,\mathrm{ISO}}^{(3.6)}$ (μJy)	$\sigma_{\mathrm{ISO}}^{(3.6)}$ (μJy)	$f_{\nu,\mathrm{AUTO}}^{(3.6)}$ (μJy)	$\sigma_{\mathrm{AUTO}}^{(3.6)}$ (μJy)	$f_{\nu,4''}^{(3.6)}$ (μJy)	$\sigma_{4''}^{(3.6)}$ (μJy)	$f_{\nu,6''}^{(3.6)}$ (μJy)	$\sigma_{6''}^{(3.6)}$ (μJy)	$f_{\nu,\mathrm{ISO}}^{(4.5)}$ (μJy)	$\sigma_{\mathrm{ISO}}^{(4.5)}$ (μJy)	$f_{\nu,\mathrm{AUTO}}^{(4.5)}$	$\sigma_{\mathrm{AUTO}}^{(4.5)}$ (μJy)	$f_{\nu,4''}^{(4.5)}$ (μJy)	$\sigma_{4''}^{(4.5)}$ (μJy)	$f_{\nu,6''}^{(4.5)}$ (μJy)	$\sigma_{6''}^{(4.5)}$ (μJy)
(1)	(2)	(3)	(4)	(5)	(6)	(7)	(8)	(9)	(10)	(11)	(12)	(13)	(14)	(15)	(16)	(17)	(18)	(19)
100020	3	2	0	0	0	0	0	0	0	0	529	8.89	528	9.23	395	3.14	474	4.09
100021	0	0	2.94	0.903	7.83	4.48	3.94	1.34	4.06	2.33	1.06	0.884	−0.863	4.47	2.14	1.32	2.93	2.32
100022	2	2	2.87	1.29	3.54	4.73	3.65	1.32	3.73	2.31	5.37	1.3	6.02	4.73	7.6	1.35	7.79	2.32
100023	1	1	4	1.31	4.04	2.04	3.03	1.33	4.67	2.33	5.94	1.15	7.72	1.78	7.25	1.18	8.22	2.03
100024	1	0	0	0	0	0	0	0	0	0	24.4	2.32	23.2	3.43	31.4	1.51	28	2.41
100025	0	0	3.38	0.898	15.7	3.85	6.51	1.34	11.6	2.33	1.01	0.873	−3.61	3.81	0.423	1.3	−2.04	2.29
100026	1	0	0	0	0	0	0	0	0	0	2.67	0.54	3.52	1.01	4.62	1.17	4.44	2.02
100027	1	1	0	0	0	0	0	0	0	0	0	0	0	0	0	0	0	0
100028	1	0	0	0	0	0	0	0	0	0	3.16	0.792	3.74	1.93	4.47	1.33	3.16	2.31
100029	1	0	0	0	0	0	0	0	0	0	7.98	1.33	6.38	2.53	10.7	1.38	9.06	2.34
100030	3	3	16.4	3.01	21.2	5.86	12.3	1.67	16.4	2.89	9.7	2.45	4.07	4.76	7.64	1.36	7.77	2.34
100031	1	1	0	0	0	0	0	0	0	0	0	0	0	0	0	0	0	0
100032	3	3	68.3	4.2	74.9	6.91	56.2	1.65	60.7	2.52	73.5	4.2	75	6.91	61.5	1.68	66.2	2.54
100033	1	0	0	0	0	0	0	0	0	0	2.55	0.547	6.13	1.21	8.2	1.36	8.53	2.35
100034	1	1	0	0	0	0	0	0	0	0	0	0	0	0	0	0	0	0
100035	0	0	0.787	0.37	6.71	1.95	5.44	1.34	8.56	2.34	0.86	0.373	1	1.93	1.78	1.32	−0.328	2.31
100036	2	2	159	5.34	158	5.84	145	2.09	151	2.85	135	4.11	135	4.47	127	1.82	133	2.33
100037	3	3	8.98	1.64	11.1	5.33	11.4	1.38	11.2	2.34	7.24	1.62	7.34	5.31	8.96	1.36	8.64	2.33
100038	0	0	23.4	2.43	26.3	5.47	26.1	1.74	27.7	2.9	14.6	2.29	14	5.2	15.4	1.61	17.1	2.74
100039	2	2	12.2	1.93	10.4	5.39	12.1	1.38	15.1	2.36	12.6	1.93	10.2	5.37	12.9	1.39	17.8	2.36
100040	1	0	0	0	0	0	0	0	0	0	11.9	1.92	11.7	3.93	14.4	1.74	14.4	2.99
100041	1	0	0	0	0	0	0	0	0	0	25.7	1.88	27.7	0.714	30.5	1.5	30.2	2.42

Note. The full table is published in its entirety at http://irsa.ipac.caltech.edu/data/SPITZER/SHELA/catalogs. This is a portion of the full table to provide form and guidance. (1) Object ID number in Table 7, (2) SExtractor flags in the 3.6 μm image, (3) SExtractor flags in the 4.5 μm image, (4) isophotal flux in the 3.6 μm image, (5) error on isophotal flux, (6) total (Kron) flux in 3.6 μm image, (7) error on total flux, (8) 3.6 μm flux measured in 4″-diameter aperture, corrected to total, (9) error on 4″-diameter flux, (10) 3.6 μm flux measured in 6″-diameter aperture, corrected to total, (11) error on 6″-diameter flux, (12) isophotal flux in the 4.5 μm image, (13) error on isophotal flux, (14) total (Kron) flux in 4.5 μm image, (15) error on total flux, (16) 4.5 μm flux measured in 4″-diameter aperture, corrected to total, (17) error on 4″-diameter flux, (18) 4.5 μm flux measured in 6″-diameter aperture, corrected to total, (19) error on 6″-diameter flux.

Table 12
Column Definitions in SHELA/SDSS-matched Catalog

Catalog Column Name[a]	Table Column Name[b]	Description	Units	Data Type
SHELA_ID	ID	Unique ID from the SHELA catalog in Table 7	…	long int
SDSS_ID	SDSS ID	ID of object in the SDSS catalogs	…	64-bit long int
SDSS_RA	SDSS R.A.	R.A. (J2000) of object in the SDSS catalog	deg	double
SDSS_DEC	SDSS decl.	decl. (J2000) of object in the SDSS catalog	deg	double
TYPE	…	Object type from SDSS catalog[c]	…	int
FLAGS	SDSS FLAGS	SDSS Flags for the object	…	64-bit long int
U[d]	**u**	SDSS *u* total AB magnitude corrected for Galactic extinction	mag	float
UERR	σ_u	uncertainty on SDSS *g* AB magnitude	mag	float
G[d]	**g**	SDSS *g* total AB magnitude corrected for Galactic extinction	mag	float
GERR	σ_g	uncertainty on SDSS *g* AB magnitude	mag	float
R[d]	**r**	SDSS *r* total AB magnitude corrected for Galactic extinction	mag	float
RERR	σ_r	uncertainty on SDSS *r* AB magnitude	mag	float
I[d]	**i**	SDSS *i* total AB magnitude corrected for Galactic extinction	mag	float
IERR	σ_i	uncertainty on SDSS *i* AB magnitude	mag	float
Z[d]	**z**	SDSS *z* total AB magnitude corrected for Galactic extinction	mag	float
ZERR	σ_z	uncertainty on SDSS *z* AB magnitude	mag	float

Notes.
[a] Column name in binary FITS tables.
[b] Column name in Table 13, if different from column name in binary FITS table.
[c] The most common type values are TYPE = 3 for Galaxy or TYPE = 6 for Star.
[d] The source SDSS magnitudes have the extension _MAG in the catalogs on IRSA.

SHELA sources are included in the catalog, and we include only the closest source in the cases where multiple SDSS sources are located within 1″ of a given SHELA source.

Table 6 provides a description of each column name in the tables and the binary FITS tables. Table 7 contains object astrometry and quantities measured from the detection image and weight maps. Tables 8–11 present the SHELA catalogs for the data release. This includes a catalog for the full, combined 3-epoch data (Table 8) and catalogs for each individual epoch (Tables 9–11). The full catalogs are provided as binary tables in Flexible Image Transport System (FITS, Hanisch et al. 2001) format.

The SExtractor flags (FLAGS (3.6 μm) and FLAGS (4.5 μm)) are stored as bits and coded in decimal as the sum of powers of 2 ($2^{\rm bit}$) for bits that are flagged. Common flag bit values are the following:

bit 1 the object has bright neighbors that may bias the photometry, or the object has more than 10% of its pixels flagged as bad or have zero weight;
bit 2 the object was deblended from another object.

Neither flag bit value is fatal, but users may require a more thorough vetting of these sources depending on their needs. Other, higher (very uncommon in the SHELA catalogs) bit values denote objects whose photometry is dubious. These objects should likely be excluded from use. These bits are available in the SExtractor User's Manual (v2.13).

The column descriptions for the binary FITS table and table for the merged SHELA–SDSS Stripe 82 catalog are listed in Table 12. Table 13 presents the photometric data for the merged SHELA–SDSS Stripe 82 catalog.

In the catalogs, objects with no coverage (in a given wavelength and/or epoch) will have weight =0 and zero flux density and error. These objects also have SExtractor bit =1 set in their flag values. The catalogs and images are available as part of this publication through IRSA, see footnote 18.

Because sources are detected in the weighted sum combination of the IRAC 3.6 and 4.5 μm data, the catalogs contain different numbers of sources detected in 3.6 μm and 4.5 μm individually. Table 14 provides the number of sources detected in different combinations of the 3.6 and 4.5 μm bands based on the requirement that sources be detected in *at least* one of the two channels with significance S/N $\geqslant$ 3. The table shows the number of sources for the S/N defined in different apertures. Clearly, the 4″-diameter apertures provide S/N $\geqslant$ 3 for the most sources. This is expected as this aperture encompasses ∼75% of the light for unresolved objects, while containing the fewest low S/N pixels. Therefore for objects whose light is well contained with 4″-diameters, we recommend this catalog as it maximizes the S/N. Catalog users can determine if the 4″-diameter aperture is too small by comparing the flux densities measured in this aperture and those in larger apertures (the 6″-diameter aperture and the Kron, _AUTO aperture, for example), and make decisions about aperture choice for their specific requirements.

5. A MODICUM OF SCIENCE

5.1. Number Counts

Galaxy number counts provide tests of galaxy evolution and cosmology (e.g., Peebles 1993). The number counts are the integral over the luminosity function and distance (redshift), containing the total contribution of galaxies of a given luminosity and distance to the cosmic background emission. The galaxy number counts in the mid-IR are particularly useful as they contain information about stellar-mass growth, dust–obscured populations, and AGN. Galaxy number counts with *Spitzer* have demonstrated the abundance of faint sources attributed to (rest-frame) near-IR and mid-IR emission from distant galaxies and their contribution to the IR background (e.g., Dole et al. 2004; Fazio et al. 2004a; Papovich et al. 2004; Sanders et al. 2007; Ashby et al. 2009, 2013a; Mauduit et al. 2012).

Table 13
SDSS Stripe 82 Coadd Photometry for Sources Matched to SHELA

ID	SDSS ID	SDSS R.A. (deg)	SDSS decl. (deg)	TYPE	SDSS FLAGS	u (mag)	σ_u (mag)	g (mag)	σ_g (mag)	r (mag)	σ_r (mag)	i (mag)	σ_i (mag)	z (mag)	σ_z (mag)
(1)	(2)	(3)	(4)	(5)	(6)	(7)	(8)	(9)	(10)	(11)	(12)	(13)	(14)	(15)	(16)
100020	8647474690342256787	17.701219	−1.132932	3	103347650576	19.377	0.016	18.439	0.004	17.740	0.003	17.434	0.003	17.175	0.006
100024	8647474690341142937	15.221294	−1.125124	6	34628174080	24.438	0.551	21.697	0.025	20.347	0.009	19.601	0.007	19.192	0.014
100029	8647474690343175313	19.864137	−1.127867	3	2450547277824	22.385	0.151	22.097	0.066	21.192	0.029	20.948	0.037	20.984	0.123
100036	8647474690342650333	18.621063	−1.131875	3	103347650560	22.802	0.243	21.048	0.027	19.731	0.009	19.213	0.010	18.837	0.019
100038	8647474690342651302	18.717668	−1.128721	3	70439879574360	25.901	3.217	24.574	0.547	23.981	0.294	23.269	0.231	22.215	0.290
100041	8647474690343175190	19.928157	−1.128586	3	68987912448	27.804	3.907	23.321	0.116	21.927	0.031	21.062	0.023	20.654	0.051
100044	8647474690342258061	17.794618	−1.127763	3	68987912448	23.361	0.328	22.871	0.114	21.835	0.042	21.323	0.039	21.003	0.095
100048	8647474690342782172	18.936888	−1.128068	3	281543964622848	24.181	0.547	23.570	0.170	23.485	0.150	23.571	0.253	24.049	1.245
100049	8647474690342717098	18.867537	−1.128079	3	68987912448	26.888	3.737	23.853	0.183	23.418	0.112	22.700	0.091	22.371	0.220
100052	8647474690341797917	16.668147	−1.135992	3	34628173840	16.636	0.003	15.029	0.003	14.560	0.003	14.510	0.003	14.477	0.003

Note. The full table is published in its entirety at http://irsa.ipac.caltech.edu/data/SPITZER/SHELA/catalogs. This is a portion of the full table to provide form and guidance. (1) Object ID number in Table 7, (2) SDSS ID number, (3) SDSS right ascension (J2000) in decimal degrees, (4) SDSS declination (J2000) in decimal degrees, (5) SDSS Type (common values are Type = 3 for galaxy and Type = 6 for star), (6) SDSS Flags value, (7) SDSS u magnitude, (8) error on u magnitude, (9) SDSS g magnitude, (10) error on g magnitude, (11) SDSS r magnitude, (12) error on r magnitude, (13) SDSS i magnitude, (14) error on i magnitude, (15) SDSS z magnitude, (16) error on z magnitude.

Table 14
Number of SHELA/IRAC Sources Detected in Different Channel Combinations

	Channel Combination					
Aperture	$S/N_1 \geqslant 3$	$S/N_2 \geqslant 3$	$S/N_1 \geqslant 3 \vee S/N_2 \geqslant 3$	$S/N_1 \geqslant 3 \wedge S/N_2 \geqslant 3$	$S/N_1 \geqslant 3 \wedge S/N_2 < 3$	$S/N_1 < 3 \wedge S/N_2 \geqslant 3$
(1)	(2)	(3)	(4)	(5)	(6)	(7)
4ARCS	1,729,650	1,701,167	1,982,997	1,447,820	207,981	181,398
6ARCS	1,329,326	1,290,800	1,564,399	1,055,727	214,091	176,862
ISO	1,677,349	1,618,215	1,946,029	1,349,535	254,104	197,157
AUTO	1,019,486	960,500	1,267,282	712,704	255,712	194,841

Note. Column (1) "Aperture," gives the name of the extension of each aperture as it appears in Table 6. Columns (2–7) S/N_1 and S/N_2 are the signal-to-noise ratios in the IRAC 3.6 and 4.5 μm flux density for each aperture, respectively. $\wedge$ and $\vee$ are the logical AND and OR operators, respectively.

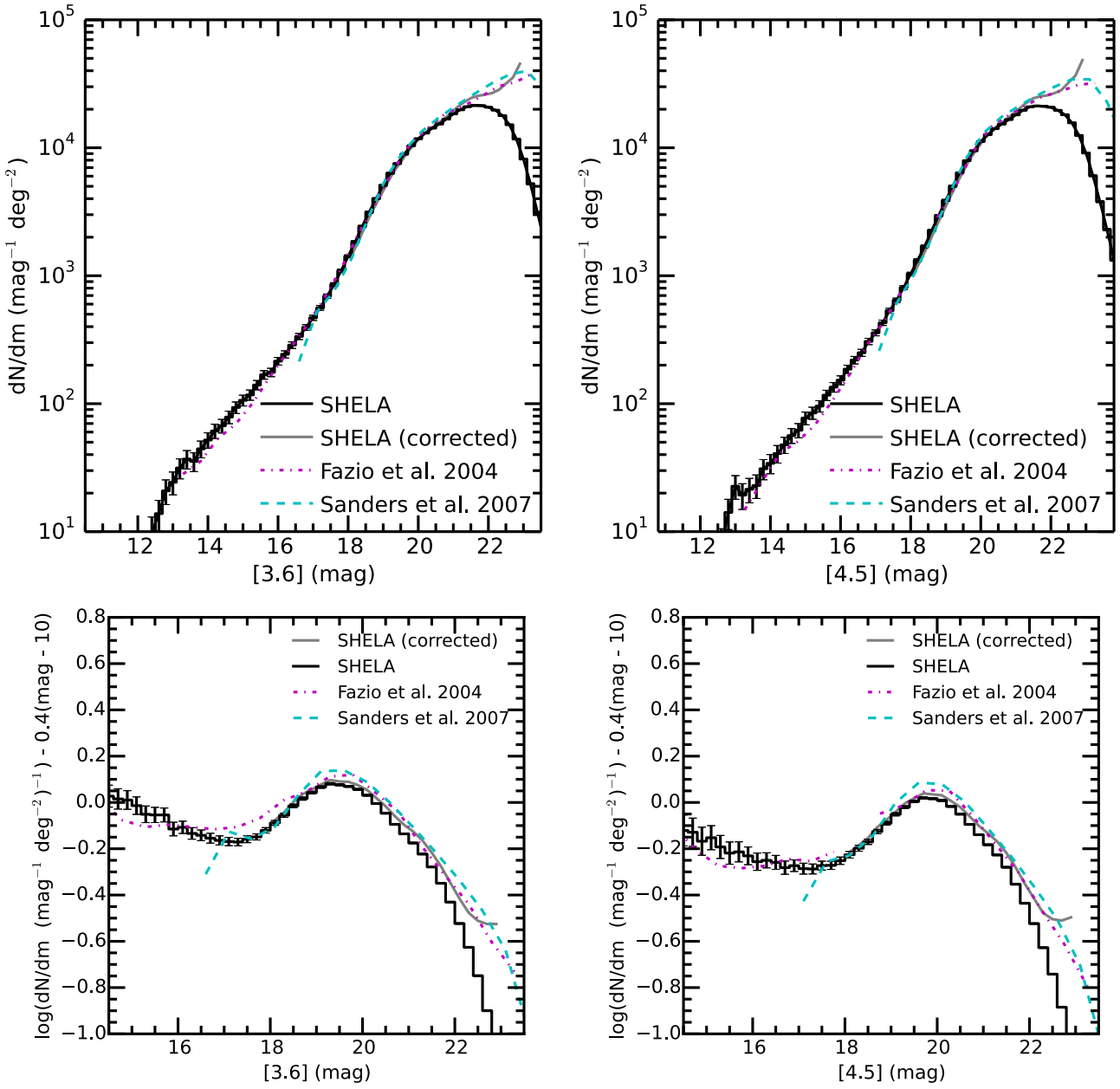

Figure 18. Top panels show the differential number counts of IRAC sources in the SHELA field in bins of 0.2 mag. The top left panel shows the results for the IRAC 3.6 μm data. The top right panel shows the results for the 4.5 μm data. The bottom panels show the differential number counts normalized to a Euclidean slope with an arbitrary offset applied.In each panel the heavy black histogram shows the IRAC counts with no correction for completeness. The error bars show Poisson uncertainties on the number counts. The gray line shows the counts corrected for incompleteness. For comparison the dashed line shows counts from S-COSMOS (Sanders et al. 2007) and the dotted–dashed line shows counts from the IRAC GTO data (Fazio et al. 2004a). The counts near the "peak" of the emission (in the lower panels) are consistent to better than 10%.

Table 15
SHELA IRAC Number Counts

m_{AB} (mag) (1)	IRAC 3.6 μm dN/dm (mag^{-1} deg^{-2}) (2)	IRAC 3.6 μm Error (mag^{-1} deg^{-2}) (3)	IRAC 4.5 μm dN/dm (mag^{-1} deg^{-2}) (4)	IRAC 4.5 μm Error (mag^{-1} deg^{-2}) (5)
12.0	7.3	1.1	3.8	0.8
12.2	7.0	1.0	3.5	0.7
12.4	9.9	1.2	6.7	1.0
12.6	13.8	1.4	7.8	1.1
12.8	20.8	1.8	14.1	1.5
13.0	24.3	1.9	22.6	1.9
13.2	31.5	2.2	19.3	1.7
13.4	36.9	2.4	21.4	1.8
13.6	35.4	2.3	22.9	1.9
13.8	44.4	2.6	31.0	2.2
14.0	52.0	2.8	34.2	2.3
14.2	61.2	3.1	40.7	2.5
14.4	67.2	3.2	47.7	2.7
14.6	78.6	3.5	56.4	2.9
14.8	93.5	3.8	62.0	3.1
15.0	106.2	4.0	77.2	3.4
15.2	117.2	4.2	84.7	3.6
15.4	140.0	4.6	95.8	3.8
15.6	168.2	5.1	116.6	4.2
15.8	175.8	5.2	134.7	4.5
16.0	215.1	5.7	152.7	4.8
16.2	243.3	6.1	186.2	5.3
16.4	287.1	6.6	219.3	5.8
16.6	335.4	7.1	250.2	6.2
16.8	394.6	7.7	306.9	6.8
17.0	469.0	8.4	358.1	7.4
17.2	561.0	9.2	429.1	8.1
17.4	693.5	10.0	533.6	9.0
17.6	853.4	11.0	643.2	9.9
17.8	1096.0	13.0	809.5	11.0
18.0	1417.0	15.0	1032.0	13.0
18.2	1839.0	17.0	1324.0	14.0
18.4	2427.0	19.0	1697.0	16.0
18.6	3138.0	22.0	2260.0	19.0
18.8	4005.0	25.0	2952.0	21.0
19.0	5088.0	28.0	3881.0	24.0
19.2	6322.0	31.0	5012.0	28.0
19.4	7523.0	34.0	6372.0	31.0
19.6	8904.0	37.0	7931.0	35.0
19.8	10390.0	40.0	9481.0	38.0
20.0	11780.0	42.0	11180.0	41.0
20.2	13040.0	45.0	12680.0	44.0
20.4	14240.0	47.0	14110.0	46.0
20.6	15330.0	48.0	15310.0	48.0
20.8	16760.0	50.0	16620.0	50.0
21.0	18400.0	53.0	18080.0	52.0
21.2	19810.0	55.0	19630.0	55.0
21.4	20950.0	56.0	20900.0	56.0
21.6	21420.0	57.0	21210.0	57.0
21.8	21360.0	57.0	21100.0	57.0
22.0	20740.0	56.0	20730.0	56.0
22.2	19680.0	55.0	19610.0	55.0
22.4	17840.0	52.0	18120.0	52.0
22.6	15140.0	48.0	15670.0	49.0
22.8	11690.0	42.0	12490.0	44.0
23.0	8166.0	35.0	9101.0	37.0

Note. (1) magnitude of number count bin, (2) number counts at 3.6 μm, (3) Poisson error on 3.6 μm number counts, (4) number counts at 4.5 μm, (5) Poisson error on 4.5 μm number counts. Note that the counts are not corrected for completeness. To do so requires dividing by the magnitude-dependent completeness corrections in Table 4.

Figure 18 shows the IRAC 3.6 and 4.5 μm number counts for the full SHELA data. The raw counts (uncorrected for completeness, see Section 4.1) are provided in Table 15. The SHELA counts agree well with previous measurements (e.g., Fazio et al. 2004a; Sanders et al. 2007). At bright magnitudes (AB $\lesssim$ 18) the counts follow roughly the expected contribution from Galactic stars (e.g., Fazio et al. 2004a; Ashby et al. 2013a and references therein). The SHELA counts show a slight excess of bright counts compared to the data in Fazio et al. and Sanders et al. This is likely a result of the different Galactic sight lines among the surveys, and is therefore not too surprising.

The counts provide an independent measure of the completeness of the SHELA IRAC catalogs. As illustrated in Figure 18, the SHELA counts agree with those of the deeper imaging in Fazio et al. (2004a) and Sanders et al. (2007) to better than 10% near the peak of the distribution. Similarly, when corrected for incompleteness (Section 4.1), the SHELA data are consistent with the counts in Fazio et al. and Sanders et al. at least down to the 50% completeness level of $m_{AB} \sim 22.5$ mag. At fainter magnitudes, the completeness corrections for the SHELA data are significantly higher and the uncertainties on the completeness corrections dominate the counts (and Eddington–type biases are most severe). Therefore, we have confidence in the completeness corrections and the number counts down to the 50% completeness limit.

5.2. Time-variable Objects

The combination of the large area and multi-epoch nature of the SHELA data set allows for the identification of sources whose brightness varies across the ~6 and 12 months baselines in time. This includes rare sources that show large changes in brightness, and sources with high proper motion (see also, Ashby et al. 2009).

As an illustration, we selected objects from the SHELA catalog that are detected in both the combined 3.6 and 4.5 μm data, have coverage in all three observing epochs, but vary by more than 2.5 mag (a factor of 10 in brightness) between any two observing epochs. There are 291 objects in the SHELA field that satisfy these requirements with [3.6] $\leqslant$ 20.5 AB mag or [4.5] $\leqslant$ 20.5 AB mag. An inspection of these objects shows they are all consistent with point sources, with several "double" (resolved, or multiple component) objects and some objects that appear to show astrometric centroid shifts between the 3.6 and 4.5 μm image (which would imply very high proper motions, indicative of asteroids). Figure 19 shows four objects that appear in only a single observing epoch. Because such objects make it into the final, three-epoch, combined catalog, care must be taken when creating object sets that require no (significant) temporal variations.

5.3. The Relation between the Scale Radius and Mass of Dark-matter Halos

The ACT survey includes the SHELA IRAC footprint, and its catalog includes SZ emission from distant ($z < 1$) clusters in the Stripe 82 field (Hasselfield et al. 2013). The thermal SZ effect is a decrement in the emission from the CMB owing to the presence of a massive (virialized) galaxy cluster along the line of sight. The hot ($T \sim 10^7$ –10^8 K) ICM gas associated with the galaxy cluster causes inverse Compton scattering of the CMB photons, leaving a distortion in the direction of the

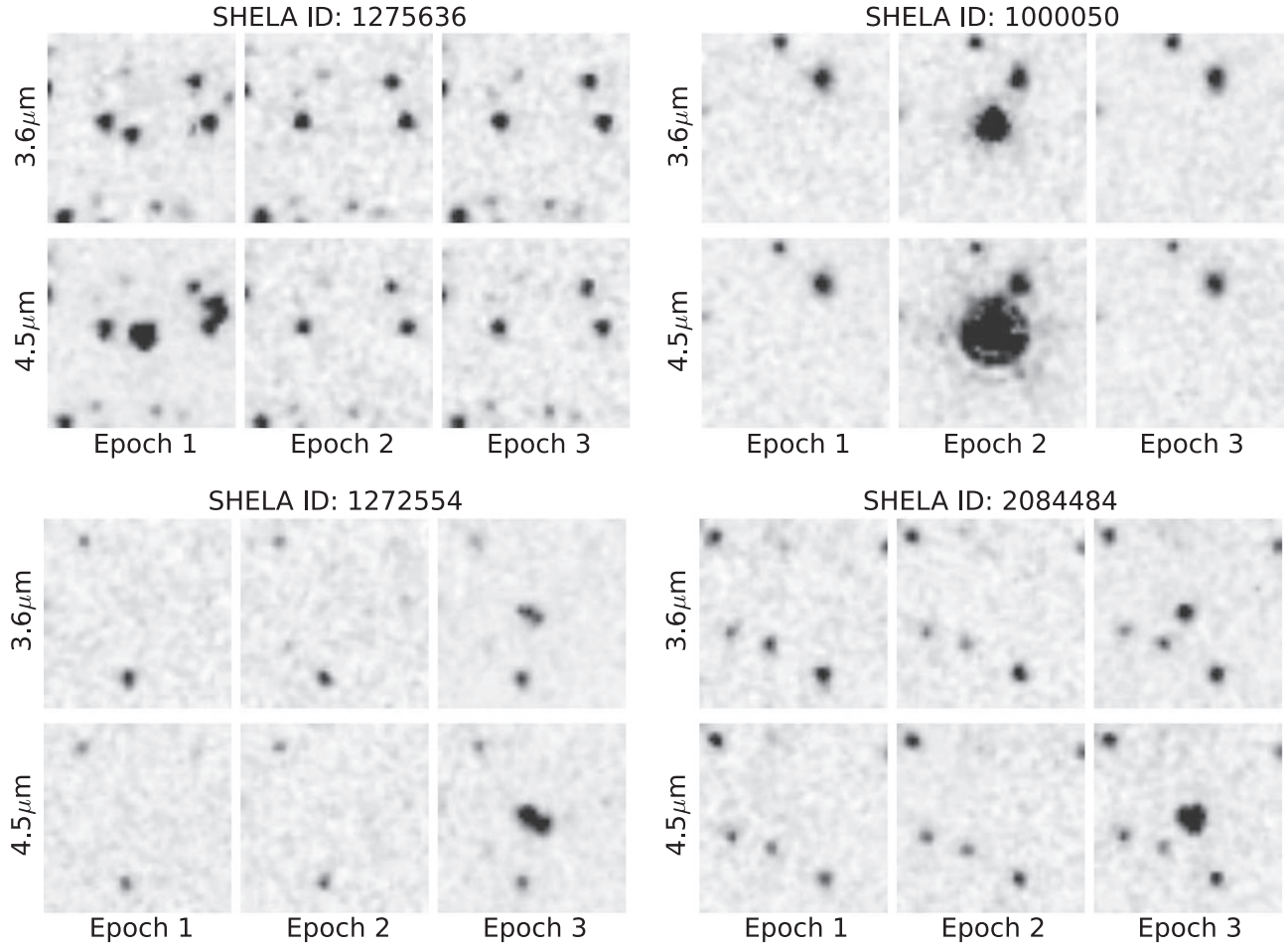

Figure 19. Examples of sources that vary in brightness by more than 2.5 magnitudes between the different SHELA observing epochs. Each set of panels shows the 3.6 and 4.5 μm images for epochs 1, 2, and 3 for 4 sources in the SHELA catalog. The object catalog IDs are given as the title for each set of plots.

cluster. The strength of the distortion is proportional to the line-of-sight integral of the thermal pressure (the Compton y parameter), which correlates with the total mass (M_{500}) associated with the galaxy cluster (e.g., Vikhlinin et al. 2009; Marrone et al. 2012; Sifón et al. 2013).

Five of the ACT clusters from Hasselfield et al. (2013) fall in the SHELA/IRAC footprint (ACT CLJ0059.1-0049, ACT CLJ0127.2+0020, ACT CLJ0119.9+0055, ACT CLJ0058.0+0030, ACT CLJ0104.8+0002). The IRAC data probe the amount of starlight associated with the galaxies in these clusters, and measure the galaxy spatial distribution. The combination of IRAC and ACT data therefore allows us to study the structural size of the dark matter halo (as traced by the galaxies in the IRAC image) and compare it with the halo mass as estimated from the SZ signal. Figure 20 shows false-color images of the five clusters in the SHELA IRAC 3.6 μm image (red-color) combined with i- and g-band images from our DECam imaging (I. Wold et al. 2016, in preparation).

Studies have shown that the surface density of satellites roughly trace the distribution of dark matter (e.g., Tal et al. 2012; Kawinwanichakij et al. 2014; van der Burg et al. 2015) predicted by the density profile of the dark matter from numerical simulations (e.g., Navarro et al. 1996 NFW hereafter). The Spitzer/IRAC data allow the measurement of the radial distribution of galaxies, and therefore a tracer of the dark matter density distribution. Following the method of Kawinwanichakij et al. (2014), we counted the number of SHELA galaxies with $17 < m_{3.6} < 22$ mag in concentric annuli centered on each cluster. To correct for the background, we measured the average (median) number of galaxies in each annulus for 10^4 randomly placed apertures around the SHELA image (taking care to avoid the image edges). We then measured the radial profile, and fit the projected NFW profile (Bartelmann 1996) using two parameters, the NFW scale angular radius, θ_s, and a normalization. The results from these fits for the NFW scale radii for each cluster are given in Table 16.

Figure 21 shows the distribution of galaxies centered on one of the ACT clusters in SHELA, ACT CLJ0058.0+0030 at $z = 0.76$. The galaxy distribution has been corrected statistically for the galaxies associated with the field as discussed above. The figure shows that the surface density of galaxies follows a projected NFW profile with a best-fit scale radius, $\theta_s = 0.51 \pm 0.14$ arcmin, which corresponds to a physical scale radius of $r_s = 223 \pm 65$ kpc (for $h = 0.7$, $\Omega_m = 0.3$, and $\Omega_\Lambda = 0.7$).

The combination of data on the radial distribution of cluster galaxies and measures of the total mass of the clusters is a potentially powerful way to study properties of dark matter halos. For an NFW profile, the scale radius is expected to increase with halo mass as $r_s \sim M_{200}^{0.45}$ (Navarro et al. 1996), where M_{200} is the mass within a radius where the density is 200

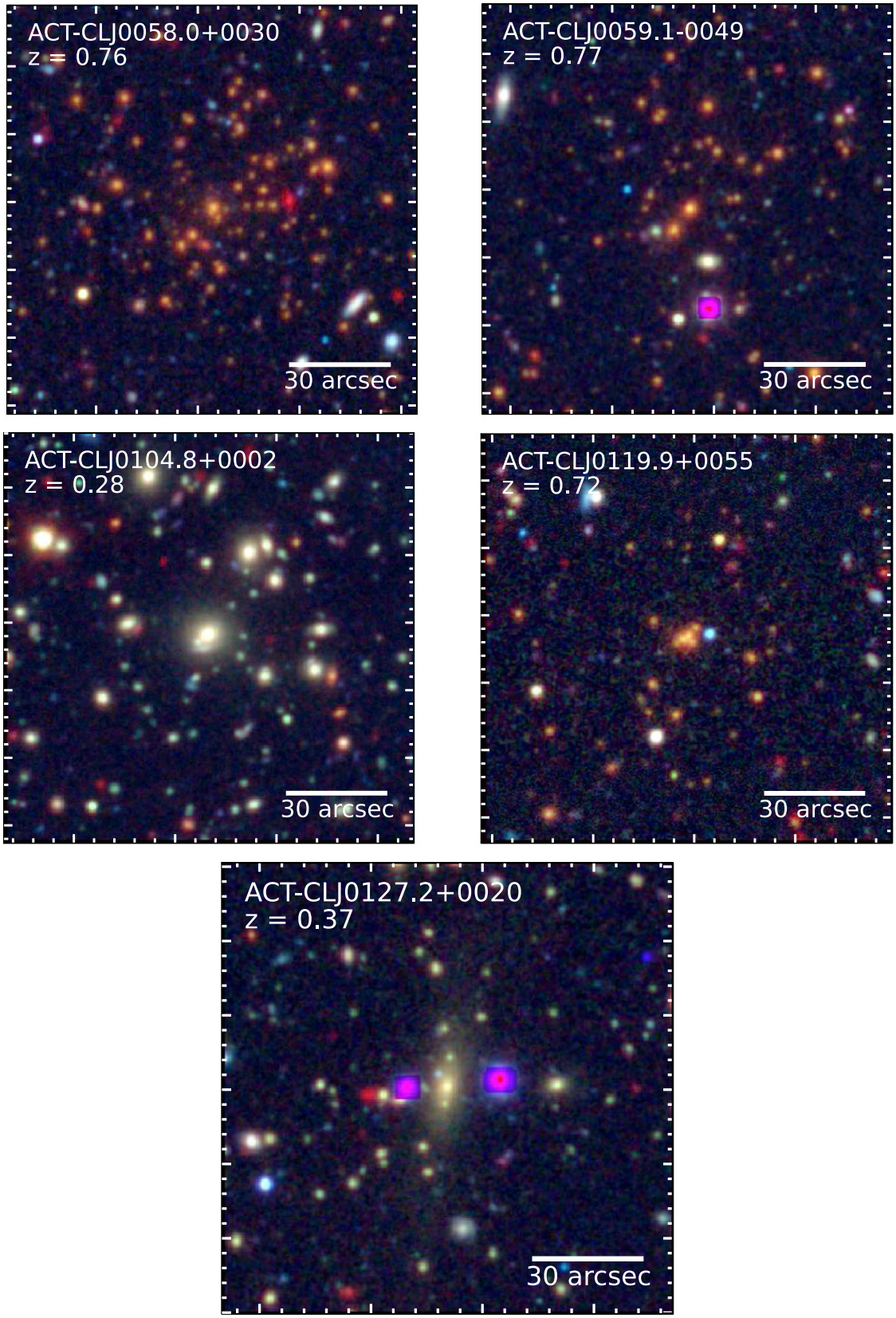

Figure 20. False-color RGB images of the five SZ-selected galaxy clusters detected in ACT that fall in the SHELA field. Each image shows a $2' \times 2'$ field centered on the astrometric position of each ACT cluster (with north up and east to the left). In each panel, the red, green, and blue colors correspond to the image from the SHELA 3.6 μm image, and DECam *i*, and *g*-bands, respectively. (The "magenta" objects are stars whose data are saturated in the DECam *i*-band images and have been masked.)

Table 16
Measures of Scale Radii of NFW profiles in ACT SZ Clusters in SHELA

Cluster	z	M_{500} (10^{14} $M_\odot$)	θ_s (arcmin)	r_s (kpc)
(1)	(2)	(3)	(4)	(5)
ACT CLJ0104.8+0002	0.28	2.6 ± 0.9	1.1 ± 0.4	280 ± 100
ACT CLJ0127.2+0020	0.37	3.3 ± 0.9	0.67 ± 0.24	205 ± 72
ACT CLJ0119.9+0055	0.72	3.3 ± 0.8	0.72 ± 0.22	311 ± 96
ACT CLJ0058.0+0030	0.76	3.2 ± 0.8	0.51 ± 0.15	223 ± 65
ACT CLJ0059.1-0049	0.77	5.2 ± 0.9	0.72 ± 0.19	318 ± 83

Note. (1) Cluster designation (from Hasselfield et al. 2013), (2) estimated redshift (from Hasselfield et al. 2013), (3) total cluster mass derived from the SZ signal (from Hasselfield et al. 2013), (4) angular scale radius θ_s of the projected NFW profile fit to the background-corrected surface density of galaxies in the SHELA IRAC data centered on each cluster, (5) scale radius converted to physical units assuming $h = 0.7$, $\Omega_m = 0.3$, and $\Omega_\Lambda = 0.7$.

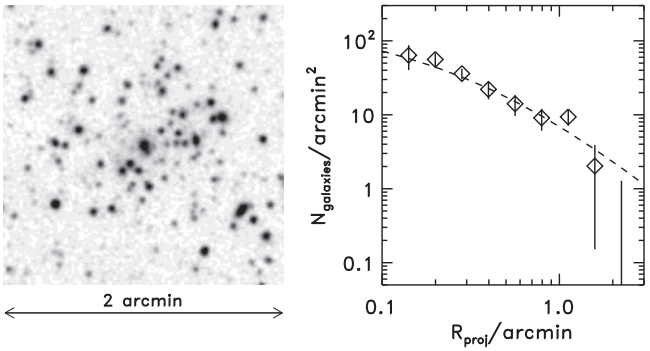

Figure 21. Left panel shows the SHELA IRAC 3.6 μm image of the ACT SZ-selected cluster CLJ0058.0+0030 at $z = 0.76$ (Hasselfield et al. 2013). The right panel shows the projected surface-density distribution of galaxies centered on the peak of the SZ signal of the cluster. The surface density is the number of galaxies in the SHELA IRAC data measured in concentric annuli centered on the cluster, corrected for the average density of galaxies in random apertures in the IRAC image. The surface density is consistent with a projected NFW profile with scale radius 0.51 ± 0.14 arcmin.

times the critical density. Simulations predict that this relation should be constant constant with redshift (e.g., Bullock et al. 2001; Eke et al. 2001; Diemer & Kravtsov 2015).

Figure 22 shows the ratio of $r_s/M_{200}^{0.45}$ for the five ACT SZ clusters in the SHELA field as a function of their redshift. The r_s values come from the projected NFW profile fits to the radial distributions of galaxies for each cluster from the IRAC catalogs (as described for CLJ0058.0+0030 in the previous paragraph). The M_{200} values come from the estimates of M_{500} from the SZ y-parameter measurements (Hasselfield et al. 2013), where we have adjusted the M_{500} values by 0.1 dex to convert them to M_{200}. Figure 22 also shows the values of $r_s/M_{200}^{0.45}$ for the simulated model halos from Navarro et al. (1996), for halos ranging from $M_{200} = 10^{13}$–10^{15} $M_\odot$. The values range from $r_s/M_{200}^{0.45} \simeq 0.1$–$0.2$ Mpc$/(10^{14}$ $M_\odot)^{0.45}$, and agree remarkably well with the observations for the 5 ACT-SZ clusters. These are consistent with the expected evolution of more modern simulations for a halo of mass 10^{13}–10^{15} $M_\odot$ (Diemer & Kravtsov 2015). The observations show indications that the shape of the dark-matter profiles has only a weak dependence on mass and redshift in accordance with predictions from ΛCDM (Bullock et al. 2001).

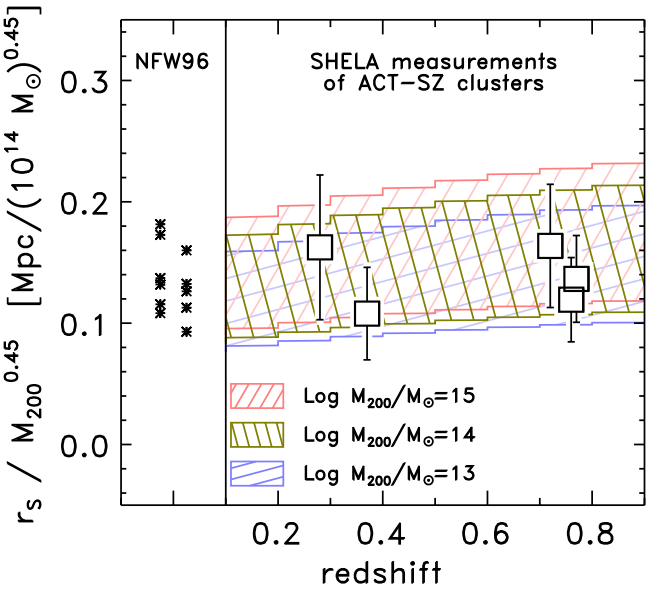

Figure 22. Evolution of the ratio between the NFW-profile scale radius, r_s and halo mass, M_{200}. The boxes and error bars show values derived for the ACT-selected clusters in SHELA. The scale radii are measured by fitting projected NFW profiles to the surface density of galaxies in each ACT cluster. The asterisks show the predicted ratio of $r_s/M_{200}^{0.45}$ for galaxy halos from NFW96. The hatched swaths show the expected ratio for halos of $\log M_{200}/M_\odot = 13$, 14, and 15 (as labeled in the figure legend) including the scatter in halo concentration using the relations in Diemer & Kravtsov (2015). The data are consistent with a near unevolving ratio of $r_s/M^{0.45}$ over a large baseline in redshift, with values consistent with DM halo scaling relations as expected from the distribution of predicted ratios for a CDM-type cosmology.

6. SUMMARY

We presented the *Spitzer* IRAC imaging at 3.6 and 4.5 μm of the SHELA survey, a *Spitzer* Exploratory program which covers a ≈24 deg^2 field within the footprint of HETDEX. This field has a rich set of multiwavelength data, including optical imaging from SDSS Stripe 82 and CTIO/DECam, near-IR imaging from NEWFIRM K-band, far-IR imaging from *Herschel*, and X-ray observations from *Chandra* and *XMM*-Newton.

The HETDEX survey will obtain redshifts in this field for ∼200,000 galaxies at $1.9 < z < 3.5$ based on Lyα emission (covering a volume of 0.5 Gpc^3), and redshifts for an additional ∼200,000 galaxies at $z < 0.5$ based on their [O II] emission. The SHELA IRAC data are sensitive to galaxies with stellar masses down to $\simeq 2 \times 10^{10}$ $M_\odot$ through the redshift range of Lyα probed by HETDEX. Thus, the combination of the HETDEX spectroscopy data, ground-based optical/near-IR imaging, and the SHELA IRAC data allow the study of the relationship between structure formation, galaxy stellar mass, dark halo mass, and environment during over a large range of cosmic history.

In this paper, we discussed the properties of the SHELA IRAC data, including the data acquisition, reduction, validation, and source catalogs. The imaging includes three observing epochs separated by approximately 6 months between epochs. The combined three-epoch data set covers 24.2 deg^2 with an exposure time of at least ≈200 s. Our tests show the images and catalogs are 80% (50%) complete to limiting magnitudes of 22.0 (22.6) AB mag in the detection image, which is constructed from the weighted-sum of the IRAC 3.6 and

4.5 μm images. The catalogs reach limiting (1σ) sensitivities of 1.1 μJy in each IRAC channel. The photometric accuracy is consistent with AllWISE with essentially no different between the [3.6] and $W1$ bands and a possible 0.02 mag offset between [4.5] and $W2$ bands.

The astrometric solution of SHELA is tied to SDSS DR7, where the astrometric uncertainty is $<0\farcs2$, comparable to the uncertainty in the SDSS catalogs. The astrometric solutions are accurate compared to 2MASS, but show a (possibly) non-negligible offset compared to AllWISE approaching one-tenth of an arcsecond.

The IRAC data enable a broad range of scientific explorations, including studies of galaxy and AGN evolution, and the formation of large-scale structure. As a demonstration of science, we present IRAC number counts, examples of highly temporally variable sources, and galaxy surface density profiles of rich galaxy clusters. At faint magnitudes, the source number counts are consistent with other IRAC data sets, which provides confidence in our estimated completeness corrections. At bright magnitudes we observe a possible excess of counts, which we attribute to variations in the surface density of Galactic stars.

We use a sample of five ACT SZ-selected galaxy clusters between $0.2 < z < 0.8$ to study the relation between cluster mass (traced by the SZ Compton parameter) and the scale radius, r_s, of the cluster halos as traced by the surface distribution of galaxies as measured from the SHELA IRAC data. All clusters show galaxy surface densities in agreement with a projected NFW halo, with a ratio of $r_s/M_{200}^{0.45}$ that is consistent with simulations of dark matter halos and is unevolving in redshift, as predicted by ΛCDM models.

In the spirit of *Spitzer* Exploratory programs we provide all images and catalogs as part of this paper. We describe the source IRAC catalogs and imaging products released for the SHELA data, which will be available through IRSA (see footnote 18).

We acknowledge useful conversations, comments and suggestions, especially from Matt Ashby, Ivo Labbé, Gordon Richards, Nick Ross, Eli Rykoff, Louis Strigari, and John Timlin. We thank Benedikt Diemer for providing his code to generate halo density profiles, and Justin Howell for comments and help incorporating the SHELA data products into IRSA. We also thank the anonymous referee for a thorough reading and constructive report. CP thanks the Space Telescope Science Institute for its hospitality and for providing a scientifically conducive atmosphere during the completion of this work. This work is based on observations made with the *Spitzer Space Telescope*, which is operated by the Jet Propulsion Laboratory, California Institute of Technology under a contract with NASA. This work is supported by the National Science Foundation through grant AST-1413317. We acknowledge generous support from the Texas A&M University and the George P. and Cynthia Woods Institute for Fundamental Physics and Astronomy. R.C., C.G., and G.Z. acknowledge support from the Institute for Gravitation and the Cosmos. The Institute for Gravitation and the Cosmos is supported by the Eberly College of Science and the Office of the Senior Vice President for Research at the Pennsylvania State University.

This work made use of data from SDSS. Funding for the SDSS and SDSS-II has been provided by the Alfred P. Sloan Foundation, the Participating Institutions, the National Science Foundation, the U.S. Department of Energy, the National Aeronautics and Space Administration, the Japanese Monbukagakusho, the Max Planck Society, and the Higher Education Funding Council for England. The SDSS Web Site is http://www.sdss.org.

The SDSS is managed by the Astrophysical Research Consortium for the Participating Institutions. The Participating Institutions are the American Museum of Natural History, Astrophysical Institute Potsdam, University of Basel, University of Cambridge, Case Western Reserve University, University of Chicago, Drexel University, Fermilab, the Institute for Advanced Study, the Japan Participation Group, Johns Hopkins University, the Joint Institute for Nuclear Astrophysics, the Kavli Institute for Particle Astrophysics and Cosmology, the Korean Scientist Group, the Chinese Academy of Sciences (LAMOST), Los Alamos National Laboratory, the Max-Planck-Institute for Astronomy (MPIA), the Max-Planck-Institute for Astrophysics (MPA), New Mexico State University, Ohio State University, University of Pittsburgh, University of Portsmouth, Princeton University, the United States Naval Observatory, and the University of Washington.

This research has made use of the NASA/IPAC Infrared Science Archive, which is operated by the Jet Propulsion Laboratory, California Institute of Technology, under contract with the National Aeronautics and Space Administration.

This research has made use of the VizieR catalog access tool, CDS, Strasbourg, France.

This publication makes use of data products from the Two Micron All Sky Survey, which is a joint project of the University of Massachusetts and the Infrared Processing and Analysis Center/California Institute of Technology, funded by the National Aeronautics and Space Administration and the National Science Foundation.

This publication makes use of data products from the Wide-field Infrared Survey Explorer, which is a joint project of the University of California, Los Angeles, and the Jet Propulsion Laboratory/California Institute of Technology, funded by the National Aeronautics and Space Administration.

REFERENCES

Abazajian, K. N., Adelman-McCarthy, J. K., Agüeros, M. A., et al. 2009, ApJS, 182, 543
Adams, J. J., Blanc, G. A., Hill, G. J., et al. 2011, ApJS, 192, 5
Alam, S., Albareti, F. D., Allende Prieto, C., et al. 2015, ApJS, 219, 12
Annis, J., Soares-Santos, M., Strauss, M. A., et al. 2014, ApJ, 794, 120
Ashby, M. L. N., Stanford, S. A., Brodwin, M., et al. 2013a, ApJS, 209, 22
Ashby, M. L. N., Stern, D., Brodwin, M., et al. 2009, ApJ, 701, 428
Ashby, M. L. N., Willner, S. P., Fazio, G. G., et al. 2013b, ApJ, 769, 80
Ashby, M. L. N., Willner, S. P., Fazio, G. G., et al. 2015, ApJS, 218, 33
Baronchelli, I., Scarlata, C., Rodighiero, G., et al. 2016, ApJS, 223, 1
Bartelmann, M. 1996, A&A, 313, 697
Beers, T. C., Flynn, K., & Gebhardt, K. 1990, AJ, 100, 32
Behroozi, P. S., Conroy, C., & Wechsler, R. H. 2010, ApJ, 717, 379
Behroozi, P. S., Wechsler, R. H., & Conroy, C. 2013, ApJL, 762, L31
Bertin, E., & Arnouts, S. 1996, A&AS, 117, 393
Bertin, E., Mellier, Y., Radovich, M., et al. 2002, in ASP Conf. Ser. 281, Astronomical Data Analysis Software and Systems XI, ed. D. A. Bohlender, D. Durand, & T. H. Handley (San Francisco, CA: ASP), 228
Blanc, G. A., Adams, J. J., Gebhardt, K., et al. 2011, ApJ, 736, 31
Blanc, G. A., Lira, P., Barrientos, L. F., et al. 2008, ApJ, 681, 1099
Bullock, J. S., Kolatt, T. S., Sigad, Y., et al. 2001, MNRAS, 321, 559
Chiang, Y.-K., Overzier, R. A., Gebhardt, K., et al. 2015, ApJ, 808, 37
Cutri, R. M., Wright, E. L., Conrow, T., et al. 2013, Explanatory Supplement to the AllWISE Data Release Products Tech. Rep

Delubac, T., Bautista, J. E., Busca, N. G., et al. 2015, A&A, 574, A59
Diemer, B., & Kravtsov, A. V. 2015, ApJ, 799, 108
Dole, H., Le Floc'h, E., Pérez-González, P. G., et al. 2004, ApJS, 154, 87
Eisenhardt, P. R. M., Brodwin, M., Gonzalez, A. H., et al. 2008, ApJ, 684, 905
Eke, V. R., Navarro, J. F., & Steinmetz, M. 2001, ApJ, 554, 114
Fazio, G. G., Ashby, M. L. N., Barmby, P., et al. 2004a, ApJS, 154, 39
Fazio, G. G., Hora, J. L., Allen, L. E., et al. 2004b, ApJS, 154, 10
Finkelstein, S. L., Hill, G. J., Gebhardt, K., et al. 2011, ApJ, 729, 140
Gawiser, E., van Dokkum, P. G., Herrera, D., et al. 2006, ApJS, 162, 1
Hagen, A., Ciardullo, R., Gronwall, C., et al. 2014, ApJ, 786, 59
Hanisch, R. J., Farris, A., Greisen, E. W., et al. 2001, A&A, 376, 359
Hasselfield, M., Hilton, M., Marriage, T. A., et al. 2013, JCAP, 7, 8
Hearin, A. P., Watson, D. F., Becker, M. R., et al. 2014, MNRAS, 444, 729
Hill, G. J., Gebhardt, K., Komatsu, E., et al. 2008, in ASP Conf. Ser. 399, Panoramic Views of Galaxy Formation and Evolution, ed. T. Kodama, T. Yamada, & K. Aoki (San Francisco, CA: ASP), 115
Ivezić, Ž, Smith, J. A., Miknaitis, G., et al. 2007, AJ, 134, 973
Jarrett, T. H., Cohen, M., Masci, F., et al. 2011, ApJ, 735, 112
Kawinwanichakij, L., Papovich, C., Quadri, R. F., et al. 2014, ApJ, 792, 103
Komatsu, E., Smith, K. M., Dunkley, J., et al. 2011, ApJS, 192, 18
Kravtsov, A., Vikhlinin, A., & Meshscheryakov, A. 2014, ApJ, submitted (arXiv:1401.7329)
Kron, R. G. 1980, ApJS, 43, 305
Kurucz, R. L. 1993, SYNTHE Spectrum Synthesis Programs and Line Data (Cambridge, MA: Smithsonian Astrophysical Observatory)
Labbé, I., Franx, M., Rudnick, G., et al. 2003, AJ, 125, 1107
Labbé, I., Oesch, P. A., Bouwens, R. J., et al. 2013, ApJL, 777, L19
Labbé, I., Oesch, P. A., Illingworth, G. D., et al. 2015, ApJS, 221, 23
LaMassa, S. M., Urry, C. M., Cappelluti, N., et al. 2013a, MNRAS, 436, 3581
LaMassa, S. M., Urry, C. M., Glikman, E., et al. 2013b, MNRAS, 432, 1351
Leauthaud, A., Tinker, J., Bundy, K., et al. 2012, ApJ, 744, 159
Lonsdale, C. J., Smith, H. E., Rowan-Robinson, M., et al. 2003, PASP, 115, 897
Marrone, D. P., Smith, G. P., Okabe, N., et al. 2012, ApJ, 754, 119
Matsuura, M., Bernard-Salas, J., Lloyd Evans, T., et al. 2014, MNRAS, 439, 1472
Matsuura, M., Zijlstra, A. A., van Loon, J. T., et al. 2005, A&A, 434, 691
Mauduit, J.-C., Lacy, M., Farrah, D., et al. 2012, PASP, 124, 714
Moster, B. P., Naab, T., & White, S. D. M. 2013, MNRAS, 428, 3121
Moster, B. P., Somerville, R. S., Maulbetsch, C., et al. 2010, ApJ, 710, 903
Muzzin, A., Marchesini, D., Stefanon, M., et al. 2013a, ApJ, 777, 18
Muzzin, A., Wilson, G., Demarco, R., et al. 2013b, ApJ, 767, 39
Navarro, J. F., Frenk, C. S., & White, S. D. M. 1996, ApJ, 462, 563
Oke, J. B., & Gunn, J. E. 1983, ApJ, 266, 713
Papovich, C. 2008, ApJ, 676, 206
Papovich, C., Dole, H., Egami, E., et al. 2004, ApJS, 154, 70
Papovich, C., Labbé, I., Quadri, R., et al. 2015, ApJ, 803, 26
Peebles, P. J. E. 1993, Principles of Physical Cosmology (Princeton, NJ: Princeton Univ. Press)
Planck Collaboration, Ade, P. A. R., Aghanim, N., et al. 2014, A&A, 571, A16
Quadri, R., Marchesini, D., van Dokkum, P., et al. 2007, AJ, 134, 1103
Reach, W. T., Megeath, S. T., Cohen, M., et al. 2005, PASP, 117, 978
Reddick, R. M., Wechsler, R. H., Tinker, J. L., & Behroozi, P. S. 2013, ApJ, 771, 30
Richards, G. T., Myers, A. D., Peters, C. M., et al. 2015, ApJS, 219, 39
Salmon, B., Papovich, C., Finkelstein, S. L., et al. 2015, ApJ, 799, 183
Sanders, D. B., Salvato, M., Aussel, H., et al. 2007, ApJS, 172, 86
Schlegel, D. J., Finkbeiner, D. P., & Davis, M. 1998, ApJ, 500, 525
Sifón, C., Menanteau, F., Hasselfield, M., et al. 2013, ApJ, 772, 25
Skibba, R. A., Coil, A. L., Mendez, A. J., et al. 2015, ApJ, 807, 152
Skrutskie, M. F., Cutri, R. M., Stiening, R., et al. 2006, AJ, 131, 1163
Slosar, A., Iršič, V., Kirkby, D., et al. 2013, JCAP, 4, 026
Somerville, R. S., & Davé, R. 2015, ARA&A, 53, 51
Springel, V., White, S. D. M., Jenkins, A., et al. 2005, Natur, 435, 629
Stetson, P. B. 1987, PASP, 99, 191
Tal, T., Wake, D. A., & van Dokkum, P. G. 2012, ApJL, 751, L5
Timlin, J. D., Ross, N. P., Richards, G. T., et al. 2016, ApJS, in press (arXiv:1603.08488)
Tinker, J., Kravtsov, A. V., Klypin, A., et al. 2008, ApJ, 688, 709
Tomczak, A. R., Quadri, R. F., Tran, K.-V. H., et al. 2014, ApJ, 783, 85
van der Burg, R. F. J., Hoekstra, H., Muzzin, A., et al. 2015, A&A, 577, A19
Viero, M. P., Asboth, V., Roseboom, I. G., et al. 2014, ApJS, 210, 22
Vikhlinin, A., Burenin, R. A., Ebeling, H., et al. 2009, ApJ, 692, 1033
Weinberg, D. H., Davé, R., Katz, N., & Hernquist, L. 2004, ApJ, 601, 1
Werner, M. W., Roellig, T. L., Low, F. J., et al. 2004, ApJS, 154, 1
Whitaker, K. E., Labbé, I., van Dokkum, P. G., et al. 2011, ApJ, 735, 86
Wilson, G., Muzzin, A., Yee, H. K. C., et al. 2009, ApJ, 698, 1943